JOURNAL OF THERMOPHYSICS AND HEAT TRANSFER
Vol. 24, No. 2, April–June 2010

Particle and Continuum Method Comparison of a High-Altitude, Extreme-Mach-Number Reentry Flow

T. Ozawa* and D. A. Levin†
Pennsylvania State University, University Park, Pennsylvania 16802
and
I. Nompelis,‡ M. Barnhardt,§ and G. V. Candler¶
University of Minnesota, Minneapolis, Minnesota 55455

DOI: 10.2514/1.42624

Stardust reentry flows have been simulated at an altitude of 80 km for a freestream velocity of 12.8 km/s using direct simulation Monte Carlo (DSMC) and computational fluid dynamics (CFD). Five ions and electrons were considered in the flowfield, and ionization processes were modeled in DSMC. The ion-averaged velocity method in DSMC was validated to maintain charge neutrality in the shock. Collision and energy-exchange models for DSMC were reviewed to ensure adequacy for the high-energy flow regime. Accurate electron-heavy particle collision cross sections and an electron-vibration relaxation model using Lee's relaxation time were implemented in DSMC. Although the DSMC results agreed well with CFD for the collision-only case, discrepancies between DSMC and CFD were observed in the shock with the relaxation model activated. Furthermore, with full chemical reactions and ionization processes, DSMC results were compared with CFD. It was found that the assumption of electron temperature is crucial for the prediction of degree of ionization. At 80 km, the degree of ionization predicted by DSMC was found to be approximately 5%, but in CFD, the degree of ionization is greater than 25% for the case of $T_e = T_{\text{tr}}$ and 9% for the case of $T_e = T_{\text{vib}}$. In DSMC, the electron-vibration relaxation model was found to be important to predict electron and vibrational temperatures at this altitude, and the electron temperature is the same order as the vibrational temperature. Therefore, compared to the DSMC solution, the assumption of $T_e = T_{\text{vib}}$ is preferable in CFD. In addition, using the Mott-Smith model, good agreement was obtained between the analytical bimodal distribution functions and DSMC velocity distributions. An effective temperature correction in the relaxation and chemical reaction models using the Mott-Smith model may reduce the continuum breakdown discrepancy between DSMC and CFD inside the shock in terms of degree of ionization and temperatures, but a general implementation is not clear.

Nomenclature

A	=	preexponential factor in Arrhenius expression
c_r	=	relative speed
E_a	=	activation energy
E_{col}	=	collision energy
Fr_i	=	fraction of the distribution function in the i direction
f_a	=	upstream Boltzmann distribution function
f_b	=	downstream Boltzmann distribution function
g	=	bimodal distribution function
K_b	=	backward reaction rate constant
K_{eq}	=	equilibrium constant
K_f	=	reaction rate constant
K_n	=	Knudsen number
k_B	=	Boltzmann constant
L	=	characteristic length
m	=	molecular mass
n	=	number density
n	=	temperature exponent in Arrhenius expression
P	=	breakdown parameter
p	=	pressure
T	=	temperature
T_i	=	temperature component in the i direction
u_i	=	mean velocity component in the i direction
v_i	=	velocity component in the i direction
Z	=	relaxation collision number
λ	=	mean free path
ν	=	collision rate
ρ	=	density
ζ	=	number of degrees of freedom
σ_T	=	total collision cross section
σ_{VHS}	=	variable hard sphere collision cross section
σ_v	=	vibrational excitation cross section
τ	=	relaxation time
τ_c	=	correction term in relaxation time
ω	=	viscosity index

Subscripts

a	=	upstream
av	=	average
b	=	downstream
center	=	center
e	=	electron
n	=	neutral
R	=	rotational mode (same as rot)

Presented as Paper 1216 at the 46th AIAA Aerospace Sciences Meeting and Exhibit, Reno, NV, 7–10 January 2008; received 9 December 2008; revision received 7 November 2009; accepted for publication 22 November 2009. Copyright © 2009 by the American Institute of Aeronautics and Astronautics, Inc. All rights reserved. Copies of this paper may be made for personal or internal use, on condition that the copier pay the $10.00 per-copy fee to the Copyright Clearance Center, Inc., 222 Rosewood Drive, Danvers, MA 01923; include the code 0887-8722/10 and $10.00 in correspondence with the CCC.

*Postdoctoral Fellow, Department of Aerospace Engineering, 135 Hammond Building; currently Project Researcher, Aerospace Research and Development Directorate, Japan Aerospace Exploration Agency, 7-44-1 Jindaiji Higashi, Chofu, Tokyo 182-8522 Japan; ozawa.takashi@jaxa.jp. Member AIAA.

†Professor, Department of Aerospace Engineering, 233 Hammond Building; dalevin@psu.edu. Associate Fellow AIAA.

‡Postdoctoral Research Associate, Department of Aerospace Engineering, 320 Akerman Hall. Member AIAA.

§Research Assistant, Department of Aerospace Engineering and Mechanics; currently Research Scientist, ELORET Corp., Sunnyvale, California 94086. Member AIAA.

¶Professor, Department of Aerospace Engineering, 119B Akerman Hall.

T = translational mode (same as tr)
V = vibrational mode (same as vib)

Superscripts

cont = continuum
part = particle

I. Introduction

THE Stardust spacecraft is one of the crucial projects of planetary and solar system exploration, returning to Earth in January 2006 after collecting dust and carbon-based samples during its closest encounter with the comet Wild 2. With the fastest reentry speed ever achieved by a man-made object at 12.8 km/s, Stardust generated a strong shock ahead of its blunt body. These shock conditions create an extremely high-temperature region in which ions and electrons are generated by ionization processes [1]. The ions and electrons lead to complicated reactions among charged and neutral particles, which further affect nonequilibrium atomic and molecular energy distributions and radiation behavior. The ionized aerothermodynamics may significantly impact the Stardust thermal protection layer ablation behavior, which is critical to the Stardust heat shield design and efficiency [2,3]. Olynick et al. [4] applied a continuum Navier–Stokes flow solver loosely coupled to radiation and material thermal ablation models to predict the Stardust reentry flows at altitudes of 43–80 km. In previous works by Ozawa et al. [1,5,6], transitional, ionized reentry hypersonic flows have been simulated using the direct simulation Monte Carlo (DSMC) method at altitudes between 68.9 and 100 km. Because of the high reentry speeds of approximately 13 km/s, the modeling of charged species and the inclusion of ionization processes to augment neutral species nonequilibrium chemical reactions challenged the DSMC method. It was found that charge neutrality can be assumed in the bow-shock region because the Debye length is very small. The ion-averaged velocity (IAV) method [1,7] was found to be sufficiently accurate when compared with an exact charge-neutrality method. The ionization reaction rates of Park [18] were adapted for use in the usual DSMC total collision energy (TCE) chemistry model. In addition, collision and energy-exchange models for DSMC were reviewed to ensure adequacy for the high-energy flow regime. The variable hard sphere (VHS) model [8] parameters were revisited to use high-temperature viscosity data because it was found that the shock thickness for an artificial gas consisting only of atomic N is sensitive to the viscosity model used in the total collision cross section. The temperature correction of Park [9,10], frequently used in continuum calculations, was implemented to ensure that the rotational and vibrational collision numbers converged to a single value for very high shock translational temperatures at which strong coupling between these two internal modes will occur. The electron-vibration (e-V) relaxation model of Lee [26] was implemented in the DSMC calculations to model the enhanced transfer of internal energy to N_2 due to the 2.3 eV shape resonance. The prediction of the electron and vibrational flowfield temperatures were found to be sensitive to the e-V relaxation model. In DSMC, the degree of ionization (DOI) increases for lower altitudes with values of 1, 4, and 11% for 100, 80, and 68.9 km, respectively. Furthermore, the DSMC solutions were compared with computational fluid dynamics/data parallel line relaxation (CFD/DPLR) results at 80 km. It was found that DSMC predicted a lower degree of ionization than CFD, and DSMC predicted lower energy-exchange rates between translational and internal modes than CFD. The following two factors were considered for the discrepancy between DSMC and CFD. First, the assumption of electron temperature was found to be very crucial in CFD because electron impact ionization reactions are very important in the flowfields and sensitive to T_e. In CFD(DPLR), electron temperature was assumed to be the same as translational temperature. However, in DSMC, electron temperature was the same order as the vibrational temperature. Second, the breakdown effect was not negligible for the Stardust reentry case. The reasons for CFD failure to correctly resolve the bow-shock structure due to continuum breakdown [11] are discussed in [12,13].

For a continuum model to be valid in a strong shock condition, it needs to fulfill the conditions of two parameters, Knudsen number and breakdown parameter [11,14]. The Knudsen number is obtained by $K_n = \lambda/L$, where L is a characteristic length. The freestream Knudsen numbers at altitudes of 68.9, 80, and 100 km are listed in Table 1 and at altitudes approximately lower than 80 km, $K_{n,\infty} < 0.01$. The continuum model breaks down with the initial symptom being that the pressure tensor becomes anisotropic if the density gradient is too high. The breakdown parameter is calculated from the expression of [8]

$$P = \frac{1}{\nu}\left|\frac{D(\ell_n(\rho))}{Dt}\right| \tag{1}$$

Figure 1 shows the breakdown parameter for the Stardust blunt body at three altitudes along the stagnation line. At 68.9 km, because of the high gradient, a sharp peak of approximately 0.5 near the body is shown. At 80 km, the maximum value is approximately 0.45, and may be contrasted with a value of P of 0.02 [8], the value at which the continuum assumption begins to fail. At 100 km, because of the low density, the maximum becomes as high as 1.0; thus, continuum models do not apply at this altitude. Therefore, for the flow for the Stardust blunt body at these three altitudes along the stagnation line, a kinetic model may be required.

In this work, we discuss the validation of continuum and particle methods for the Stardust reentry simulations by comparing the DSMC [8] with a CFD code [15,16]. The DSMC method has been developed to simulate the ionized hypersonic flows in front of a Stardust blunt body at altitudes between 68.9 and 100 km. The effect of collision processes, energy-exchange processes, and chemical reaction processes on the overall flowfield is investigated, and we estimate the difference between the DSMC and CFD predictions in a transitional regime. In this work, the electron temperature in CFD is set to be the same as either the translational temperature or vibrational temperature. In addition, we propose a correction model for use in CFD to minimize the effect of breakdown by studying the DSMC velocity distribution functions.

II. Modeling of Ionization

The most widely used chemical reaction model in DSMC is the TCE model [8,17]. In our work, ionization processes are treated as chemical reactions; thus, the TCE model is used for these processes as well. In this model, the reaction probability has a special form that allows one to match experimental reaction rates $K_f(T)$ in modified Arrhenius form, $K_f = AT^n \exp(-E_a/k_BT)$. If one of the reactants is an electron, the rate is a function of electron temperature T_e. The backward rates (i.e., ion recombination rates) can be expressed from the principle of detailed balances as $K_b = K_f/K_{\text{eq}}$, where K_b is the backward rate, K_f is the forward rate, and K_{eq} is the equilibrium constant for the reaction. The ionization processes that will be considered in the flow are listed in Table 2 [18]. For electron impact ionization processes $e^- + N \rightarrow e^- + N^+ + e^-$ (4) and $e^- + O \rightarrow e^- + O^+ + e^-$ (5) to be used in the TCE model, the temperature exponent, n, must be greater than -1.5. Hence, the Arrhenius parameters are modified for the required high-temperature range.

Table 1 Freestream parameters

Parameter	68.9 km	80 km	100 km
Temperature, K	224	185	181
Number density, molecule/m^3	1.6028×10^{21}	4.18×10^{20}	1.19×10^{19}
Speed, km/s	11.9	12.8	12.8
O_2 mole fraction, %	23.72	21	18
N_2 mole fraction, %	76.28	79	78
O mole fraction, %	0	0	4
$K_{n,\infty}(L = 0.22$ m)	4.1×10^{-3}	1.3×10^{-2}	5.4×10^{-1}

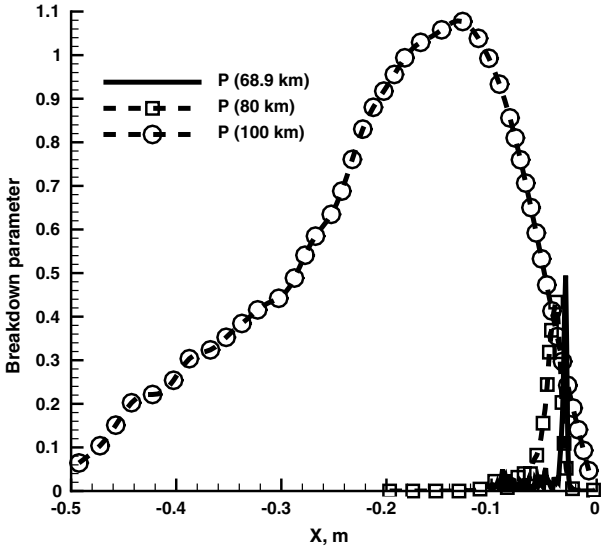

Fig. 1 Breakdown parameter for the Stardust blunt body at altitudes of 68.9, 80, and 100 km along the stagnation line.

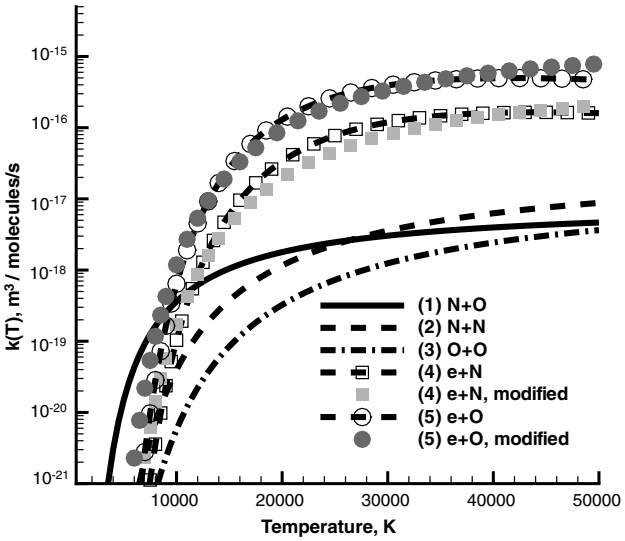

Fig. 2 Comparison of five ionization rates between 500 and 50,000 K.

Figure 2 shows that $e^- + N \rightarrow e^- + N^+ + e^-$ (4) is the highest rate at high temperature and, at lower temperature, $N + O \rightarrow NO^+ + e^-$ (1) is the initiating ionization process. It may also be seen that the agreement between the original reaction rate of Park [18] and the modified rates are in good agreement.

A. Numerical Flow Modeling Technique in Direct Simulation Monte Carlo

In the flow modeling, 11 species (N, O, N^+, O^+, N_2, O_2, NO, N_2^+, O_2^+, NO^+, and e^-) are considered for the Stardust blunt body. Figure 3 shows the Stardust blunt body geometry that is studied in this work. The freestream parameters at altitudes of 68.9, 80, and 100 km are listed in Table 1.

The DSMC method is implemented in the statistical modeling in a low-density environment (SMILE) [20,21] computational tool. In this work, a single-time-step IAV model [7] was used to model charged species in DSMC. The computational time step, Δt, is the one associated with molecular collisions rather than with the electron collision frequency. For this model, the electron movement depends on the average speed of ions in a given cell, and compared to the quasi-neutrality model of Bird [22], is computationally more efficient. In the IAV model, average ion velocities are calculated per cell and an electron velocity (or energy) is stored per simulated electron. This electron velocity is used to calculate the collision frequency, energy exchange, and chemical reaction rates between electrons and heavy particles. In DSMC, the majorant frequency scheme is employed for modeling the molecular collision frequency [21], and the VHS model is used for modeling the interaction between particles [17]. Note that collisions are modeled between electrons and neutrals and ions, but not between electrons and electrons in DSMC. The viscosity index of the electron species was set to 0.1 if not specified. The Borgnakke–Larsen (BL) model with temperature-dependent rotational and vibrational relaxation numbers was used for modeling rotation-translation (R-T) and vibration-translation (V-T) energy transfer between neutral species, and 51 chemical reactions including five ionization processes are considered [18,19] for the full set of calculations. The Millikan and White (MW) [23] form of the relaxation time is used for V-T rates, and Parker's rates [24] for the R-T rates. For high temperatures, it is known that the vibration–rotation coupling is so important that both vibrational and rotational collision numbers become a similar constant number. However, without any corrections, as temperature increases (e.g., $T > 20,000$ K), the MW vibrational collision number becomes smaller than the rotational collision number. Thus, in this work, a constant correction term of $\sigma_v = 1.0$ Å^2 is used for V-T collision numbers to be consistent with the rotational collision numbers [9,10].

In addition, e-V relaxation is modeled using the Lee's relaxation time for N_2 [25,26] From his solution he found that the maximum value of the rate coefficient for each vibrational state lies around 16,000 K [25], and that the minimum relaxation time lies around 7000 K, due to the strong shape resonance effect. The e-V collision number $Z_{\text{e-V}}$ may be related to the e-V relaxation time $\tau_{\text{e-V}}$ as

$$Z_{\text{e-V}}^{\text{cont}} = \nu \tau_{\text{e-V}}, \qquad Z_{\text{e-V}}^{\text{cont}} = n_n \overline{\sigma_T c_r} \frac{p_e \tau_{\text{e-V}}}{n_e k_B T_e} \tag{2}$$

Table 2 Ionization reactions used in the TCE model

Reaction	A, m^3/s	n	E_a, $\times 10^{-19}$ J	T	Reference
(1)$N + O \rightarrow NO^+ + e^-$	8.80×10^{-18}	0.000	4.40	T_{tr}	Park [18]
(2)$N + N \rightarrow N_2^+ + e^-$	3.39×10^{-17}	0.000	9.32	T_{tr}	Park [18]
(3)$O + O \rightarrow O_2^+ + e^-$	1.83×10^{-17}	0.000	11.1	T_{tr}	Park [18]
(4)$e^- + N \rightarrow e^- + N^+ + e^-$	4.15×10^{3}	−3.82	23.3	T_e	Park [18]
(4)$e^- + N \rightarrow e^- + N^+ + e^-$	9.00×10^{-11}	−1.00	15.0	T_e	Modified
(5)$e^- + O \rightarrow e^- + O^+ + e^-$	6.48×10^{3}	−3.78	21.9	T_e	Park [18]
(5)$e^- + O \rightarrow e^- + O^+ + e^-$	3.00×10^{-10}	−1.00	14.0	T_e	Modified
(1R)$NO^+ + e^- \rightarrow N + O$	1.494×10^{-11}	−0.65	0.00	T_e	Park [18]
(1R)$NO^+ + e^- \rightarrow N + O$	4.03×10^{-9}	−1.63	0.00	T_e	Bird [19]
(1R)$NO^+ + e^- \rightarrow N + O$	2.00×10^{-6}	−2.05	0.00	T_e	Modified
(2R)$N_2^+ + e^- \rightarrow N + N$	4.483×10^{-12}	−0.50	0.00	T_e	Park [18]
(2R)$N_2^+ + e^- \rightarrow N + N$	8.88×10^{-10}	−1.23	0.00	T_e	Bird [19]
(2R)$N_2^+ + e^- \rightarrow N + N$	1.00×10^{-8}	−1.43	0.00	T_e	Modified
(3R)$O_2^+ + e^- \rightarrow O + O$	2.49×10^{-12}	−0.50	0.00	T_e	Park [18]
(3R)$O_2^+ + e^- \rightarrow O + O$	3.83×10^{-9}	−1.51	0.00	T_e	Bird [19]
(3R)$O_2^+ + e^- \rightarrow O + O$	6.00×10^{-8}	−1.60	0.00	T_e	Modified

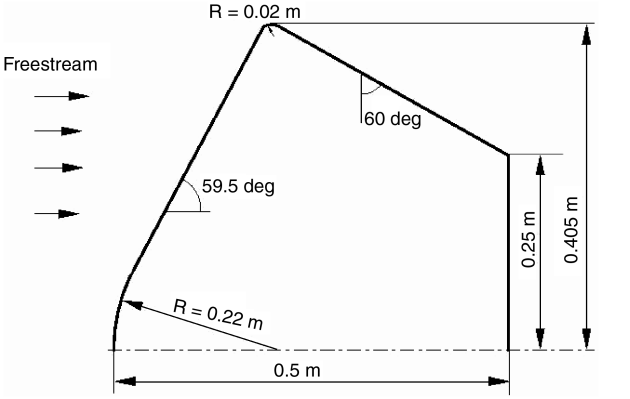

Fig. 3 Schematic of a Stardust configuration.

where $p_e\tau_{\text{e-V}}$ is given from the data of Lee [25], and the other quantities such as n_n, $\overline{\sigma_T c_r}$, n_e, and T_e are calculated in the DSMC simulation. It may be seen that $Z_{\text{e-V}}^{\text{cont}}$ is dependent on the degree of ionization and the electron temperature. Using the approach of Lumpkin et al. [27] and Haas et al. [28], the e-V collision number for use in DSMC may be obtained by

$$Z_{\text{e-V}}^{\text{part}} = \frac{\zeta_T}{\zeta_T + \zeta_V} Z_{\text{e-V}}^{\text{cont}} \tag{3}$$

More accurate parameters for the VHS model were obtained for $e^- + N$, $e^- + N_2$, $e^- + O$, $e^- + O_2$, and $e^- + NO$ collisions. The new parameters for the electron scattering cross sections are listed in Table 3. The new parameters in Table 3 are used to calculate the VHS collision cross section σ_{VHS}. For $e^- + N_2$ and $e^- + NO$, the resonance peak is not negligible; thus, further corrections are proposed for the collision cross section. For N_2, the resonance peak was added to σ_{VHS}:

$$\begin{aligned} \sigma_T(\text{Å}^2) &= \sigma_{\text{VHS}} + 22/0.7 \times (E_{\text{col}} - 1.5) \\ &\quad (1.5 \le E_{\text{col}}\ (\text{eV}) \le 2.2) \\ \sigma_T(\text{Å}^2) &= \sigma_{\text{VHS}} - 22/1.8 \times (E_{\text{col}} - 4) \\ &\quad (2.2 < E_{\text{col}}\ (\text{eV}) \le 4) \end{aligned} \tag{4}$$

where E_{col} is the collision energy. Similarly, for NO,

$$\begin{aligned} \sigma_T(\text{Å}^2) &= \sigma_{\text{VHS}} + 4/0.7 \times (E_{\text{col}} - 1.2) \\ &\quad (0.5 \le E_{\text{col}}\ (\text{eV}) \le 1.2) \\ \sigma_T(\text{Å}^2) &= \sigma_{\text{VHS}} - 4/0.8 \times (E_{\text{col}} - 2) \\ &\quad (1.2 < E_{\text{col}}\ (\text{eV}) \le 2) \end{aligned} \tag{5}$$

The TCE model [38] was used for chemical reactions for both charged and neutral species. The electric force was not included because charge neutrality was assumed. The gas-surface interaction was modeled using the Maxwell model with total energy and momentum accommodation with a surface wall temperature of 1000 K. No surface reactions are considered for comparisons with CFD.

Table 3 VHS parameters for electron scattering cross sections

Pairs	ω	σ_{ref}, Å^2	T_{ref}, K	Reference
$e^- + N$	0.19	21.0	1000	[29,30]
$e^- + N_2$	−0.10	8.0	1000	[31–33]
$e^- + O$	−0.05	7.0	1000	[29,34]
$e^- + O_2$	−0.09	5.0	1000	[35]
$e^- + NO$	0.05	11.5	1000	[36,37]

The time step, cell size, computational domain, and total number of simulated molecules were investigated to obtain results that were independent of these DSMC numerical parameters. At 80 km, approximately, 8×10^6 particles were simulated in the computational domain, and the total numbers of collision and macroparameter cells were 200,000 and 60,000, respectively. The total number of time steps was about 100,000 with a time step of 3.0×10^{-8} s for this altitude. Macroparameter sampling was started after a time step that was sufficient to reach the steady state.

B. Numerical Methods and Physical Models Used in Computational Fluid Dynamics

The axisymmetric Navier–Stokes equations with 11-species air chemistry are integrated to steady state using a finite volume method of discretization and an implicit time integration scheme [39]. The inviscid fluxes are computed using a modified Steger–Warming method [40] that is second-order accurate in space. Viscous fluxes are computed with a second-order central-difference scheme, and a formulation that is valid for the high temperatures of interest is used to compute the viscosity and thermal conductivity coefficients [41].

The transport equations for species densities, momentum, and energy are solved along with the rotational and vibrational energy transport equations for a mixture of perfect gases. Charge neutrality is required in the model. The electronic energy mode is neglected in the present work. The physical models employed for chemical reactions and energy relaxation are the same as those used in DSMC. The energy rate for V-T and R-T relaxation use a Landau–Teller model with the appropriate relaxation time constants. The Millikan and White [23] form of the relaxation time is used for the V-T rates and Parker's form [24] is used for the R-T rates. The relaxation times employ the same corrections as the DSMC for consistency. Chemical reactions for 11-species air including ionization use the rates of Park for the modified Arrhenius form of the forward reactions and the principle of detailed balance for the backward rates. These are also consistent with the DSMC rates. The $\sqrt{TT_{\text{vib}}}$ model of Park is used for vibration-dissociation coupling. Similar to the DSMC calculations, no surface reactions are modeled in CFD.

III. Results and Discussion

A. Investigation of Direct Simulation Monte Carlo Sensitivity to Collision Parameters

The influence of collision parameters on the flowfield was investigated in this high-energy range. In a previous work by Ozawa et al., the extension of parameters obtained from low-temperature data was found to cause an increased error for high temperatures [5]. Thus, new collision parameters were obtained from high-temperature viscosity data for N, N_2, O, O_2, and NO. A comparison of the viscosity index and diameter for air species, between Bird [8] (SMILE baseline parameters) and high-temperature data, is listed in Table 4. It was found that the previous collision parameters, from data given by Bird [8] (used in SMILE), predicted smaller VHS cross sections compared with the VHS cross sections obtained from high-temperature viscosity data [42–44].

The sensitivity of the DSMC flowfield to the VHS total collision cross section was investigated for a 100%-N-only case at 80 km and a

Table 4 VHS parameters

Bird				High temperature			
Species	ω	d_{ref}, Å	T_{ref}, K	ω	d_{ref}, Å	T_{ref}, K	Reference
N	0.25	2.96	273	0.15	3.11	1000	Svehla [42]
N_2	0.24	4.11	273	0.18	3.58	1000	Stallcop et al. [43]
O	0.25	2.96	273	0.15	2.96	1000	Svehla [42]
O_2	0.27	4.01	273	0.18	3.37	1000	Wright et al. [44]
NO	0.29	4.14	273	0.15	3.41	1000	Svehla [42]

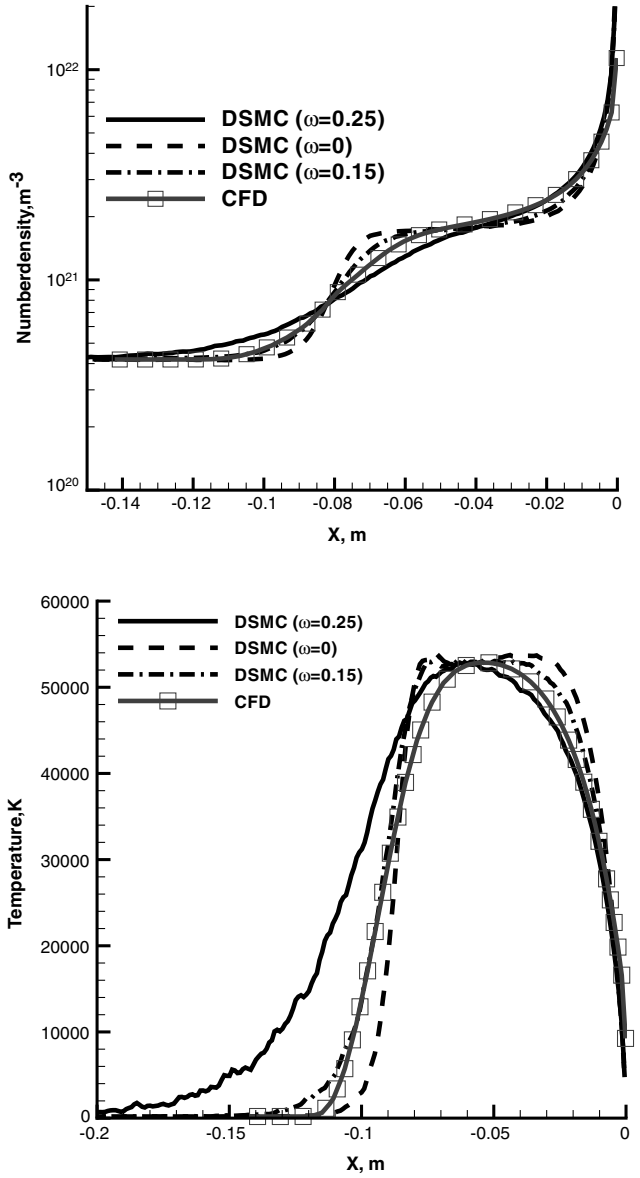

Fig. 4 Comparison of number density and translational temperature at 12.8 km/s for the Stardust blunt body at an altitude of 80 km along the stagnation line (no reactions, N only.) $\omega = 0.25$, $\omega = 0.15$ (VHS), and $\omega = 0$ (HS) are compared in DSMC.

freestream velocity of 12.8 km/s. A number density of 4.18×10^{20} m^{-3} and a freestream velocity of 12.8 km/s were used. Figure 4 presents comparisons of number density and translational temperature at 12.8 km/s for the Stardust blunt body at an altitude of 80 km along the stagnation line. Three viscosity index values of $\omega = 0.25$ and 0.15 (VHS) and $\omega = 0$ (HS) models were implemented in DSMC and compared with CFD results. It can be seen that the CFD has better agreement with the case of $\omega = 0.15$ (VHS) than the original low-temperature SMILE parameter, $\omega = 0.25$ (VHS). For high-energy flows, it is important in DSMC to use VHS parameters obtained from high-temperature viscosity data, such as that of Svehla [42]. DSMC predicts a slightly wider high-temperature region than CFD, but the maximum temperature and the profile agreed well for this case. Note that the present CFD results agree well with the CFD results calculated by the DPLR software shown earlier [15].

B. Investigation of Energy-Exchange Models for Computational Fluid Dynamics and Direct Simulation Monte Carlo

In this subsection, we investigate the energy-exchange models in DSMC and CFD. It was found that for the case of only elastic collision processes there is not any significant difference between the DSMC and CFD results. The R-T and V-T relaxations were activated in this subsection, and the differences between DSMC and CFD as well as the effect of the breakdown phenomenon are discussed. For N_2 and O_2 vibrational relaxation, a temperature-dependent collision number obtained from Millikan and White [23] with a high-temperature correction was used in DSMC and CFD. Without any corrections, the MW vibrational collision numbers become smaller than the rotational collision numbers, and this is unphysical. Thus, a high-temperature correction term is necessary. In the DSMC calculation, the vibration–rotation coupling was considered using a constant correction term of $\sigma_v = 1.0$ Å^2 [9,10], and in the CFD calculation, two correction terms are used, temperature dependent $\tau_c(T)$ and constant τ_c.

First, zero-dimensional calculations were implemented, and relaxation models between DSMC and CFD [15,16] were tested. The DSMC and CFD relaxation rates were compared with the Landau–Teller equation. Figure 5 shows that the N_2 vibrational relaxation at the initial temperature $T_0 = 10,000$ K for the adiabatic case and both DSMC and CFD results agree well with the Landau–Teller equation. For N_2 rotational relaxation, a temperature-dependent collision number obtained from Parker [24] was used in DSMC and CFD, and the relaxation rates were compared. In Fig. 6, only R-T relaxation was activated, whereas in Fig. 7, both R-T and V-T relaxations were activated. Good agreement for the R-T relaxation rate was obtained between DSMC and CFD. Both methods agree well and show faster R-T relaxation and slower V-T relaxation, as expected.

Figure 8 shows the N_2 vibrational relaxation at $T_0 = 50,000$ K for the adiabatic case. At this temperature, the high-temperature correction term is so important that it affects the V-T relaxation rate. In the CFD calculation, two correction terms are used, temperature dependent $\tau_c(T)$ and constant τ_c ($\sigma_v = 1.0$ Å^2) [9,10]. In the DSMC calculation, the vibration–rotation coupling was considered using a constant correction term of $\sigma_v = 1.0$ Å^2. Figure 8a shows a comparison between three CFD results and the Landau–Teller equation, and Fig. 8b shows a comparison between a DSMC result and the Landau–Teller equation. Three CFD results are compared, the MW relaxation rate 1) without a correction, 2) with a $\tau_c(T)$, 3) with a constant τ_c. Note that the calculated rates in CFD were compared with the Landau–Teller equation for all three cases, and they agreed well. It is shown that for the case without a correction the V-T relaxation is significantly faster than the other two cases, and the rate for case 2 is lower than that for case 3. The DSMC relaxation rate was also compared with the Landau–Teller equation, and good agreement was obtained. It is also found that the CFD result for case 3 shows good agreement with DSMC for the constant τ_c case. Therefore, for further comparisons between CFD and DSMC, we use this constant correction term, τ_c, in both methods.

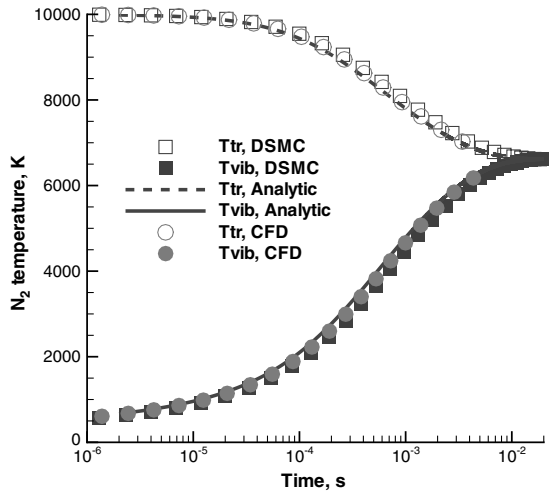

Fig. 5 Vibrational relaxation of N_2 for an adiabatic case, $T_0 = 10,000$ K.

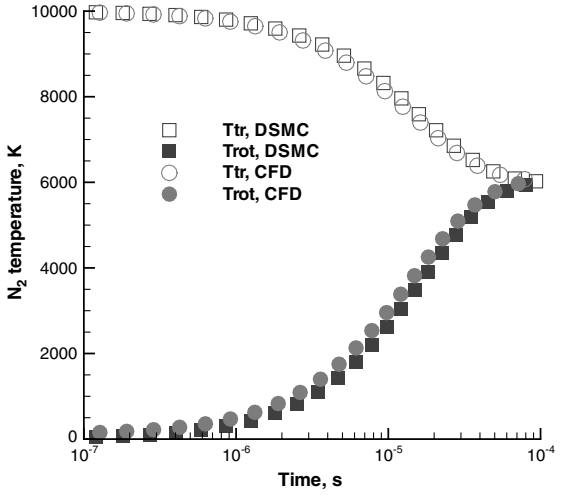

Fig. 6 Rotational relaxation of N_2 for an adiabatic case, T_0= 10, 000 K.

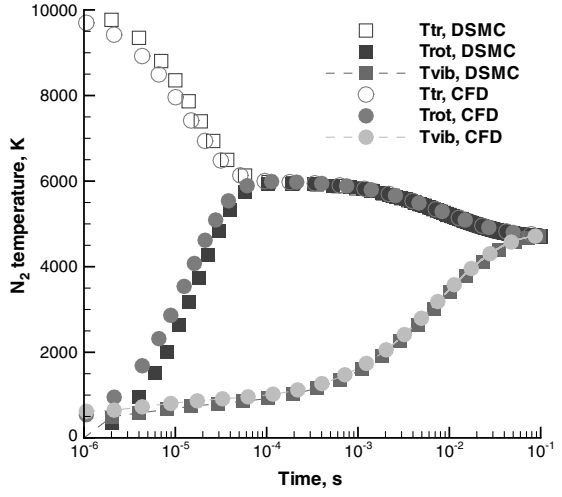

Fig. 7 Rotational and vibrational relaxation of N_2 for an adiabatic case, $T_0 = 10, 000$ K.

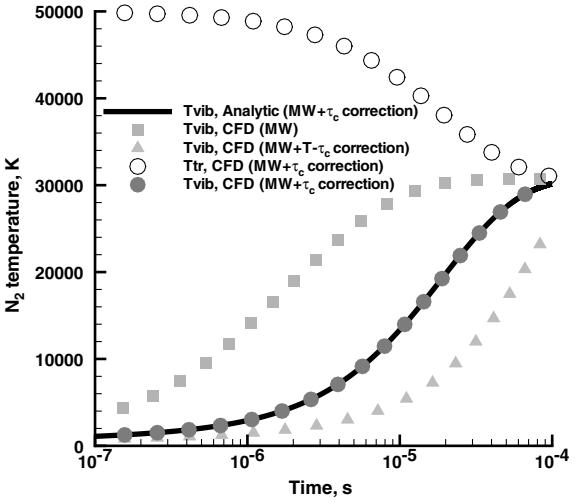

a)

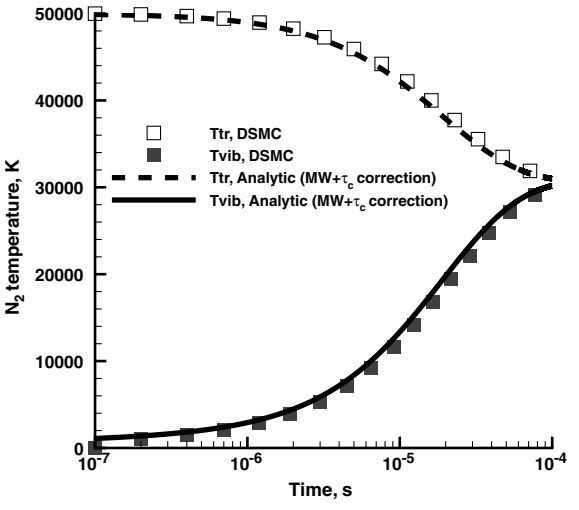

b)

Fig. 8 Vibrational relaxation of N_2 for an adiabatic case, $T_0 = 50, 000$ K: a) CFD, and b) DSMC.

Using the R-T and V-T relaxation rates that were compared between DSMC and CFD earlier, flowfield calculations were performed to test the sensitivity of the flowfield spatial dependence with respect to energy-exchange models. N_2 (79%) and O_2 (21%) were modeled with no chemical reactions. Using a total number density of 4.18×10^{20} m^{-3} and a freestream velocity of 12.8 km/s, the DSMC predictions were compared with CFD. The viscosity data for high temperatures was used in the DSMC as well [5].

Figure 9 shows comparisons of the pressure and temperatures along the stagnation line for the Stardust blunt body at an altitude of 80 km for a freestream speed of 12.8 km/s. Compared with the case of no relaxation in Fig. 4, we can see the discrepancies between the DSMC and CFD predictions for this case. Note that, similar to the previous subsection, the present CFD results were compared with DPLR, and they agreed well. CFD predicted a slightly thinner shock than DSMC, and in terms of rotational and vibrational temperatures, good agreement was obtained. However, CFD predicted much lower translational temperatures than DSMC [11]. For strong shock cases, continuum methods have been found to predict a thinner shock and underestimate the temperature overshoot phenomenon [11–13]. Differences in the DSMC and CFD results are attributed to failure of the continuum approach in regions of steep flow gradients. Compared to DSMC, CFD cannot predict the temperature overshoot phenomenon well, for example. We discuss and investigate the details of the discrepancy between DSMC and CFD in the following subsection.

C. 80 km Stardust at 12.8 km/s

The effect of chemical reactions and charged species between DSMC and CFD is discussed in this subsection. Eleven species (N, O, N^+, O^+, N_2, O_2, NO, N_2^+, O_2^+, NO^+, and e^-) cases with five ionization processes are compared between two methods and discussed for the Stardust blunt body at 80 km. For CFD, we will test the assumptions of $T_e = T_{\text{tr}}$ and $T_e = T_{\text{vib}}$, respectively, and use a three-temperature model (T_{tr}, T_{rot}, and T_{vib}). The rates of electron impact ionization processes are sensitive to electron temperature; thus, we also investigate the contribution of the two electron impact ionization processes on the overall degree of ionization. To estimate thermal protection layer ablation behavior, the prediction of heat transfer and radiation is important. For radiation calculations, the predicted electron temperature plays an important role.

Figures 10 and 11 show the normalized total number density, translational temperature, electron number density normalized by the freestream number density, and electron temperature contours in DSMC, respectively. In Fig. 10, it is seen that the shock standoff distance with regard to the high-temperature region is greater than that with respect to the high number density region. The maximum DOI is approximately 5% at 80 km, and the maximum translational temperature is between 60,000 and 70,000 K. The maximum number densities are observed at the shoulder of the Stardust body. Because of the nonequilibrium nature of the flow, the peak number of reactions can occur, not on the stagnation streamline, but on the shoulder of the body at 80 km. The peak of the electron temperature,

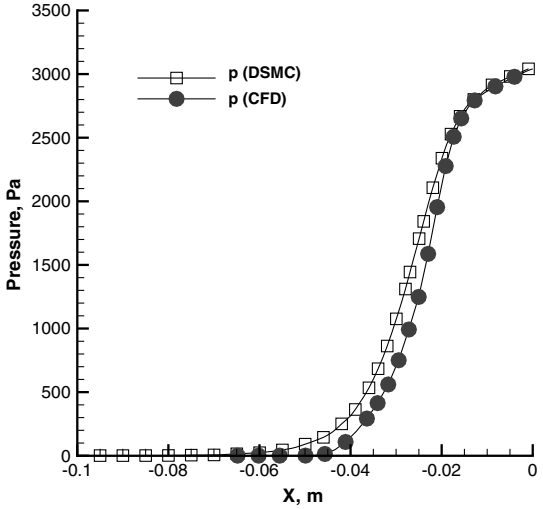

a)

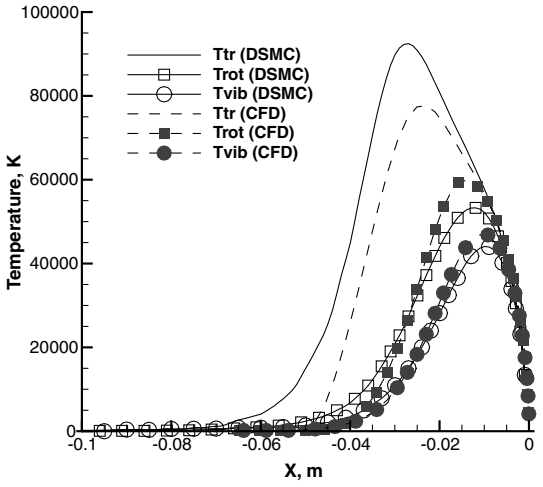

b)

Fig. 9 Stardust blunt body at an altitude of 80 km for a freestream velocity of 12.8 km/s along the stagnation line (no reactions, ω from high-temperature viscosity data): a) pressure, and b) translational, rotational, and vibrational temperatures. DSMC (MW Z_V and Z_R [23]) and CFD are compared. For the correction term, $\sigma_v = 1.0$ Å^2 for both DSMC and CFD.

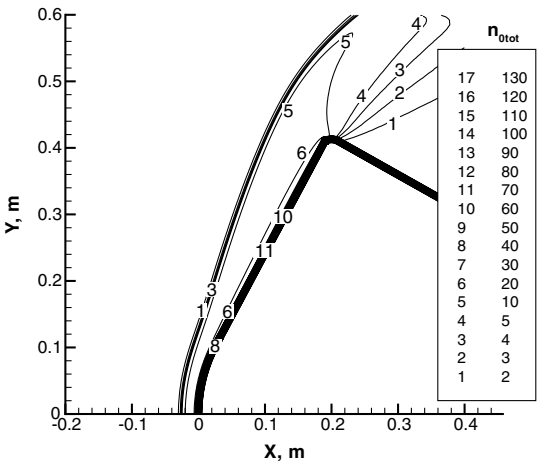

a)

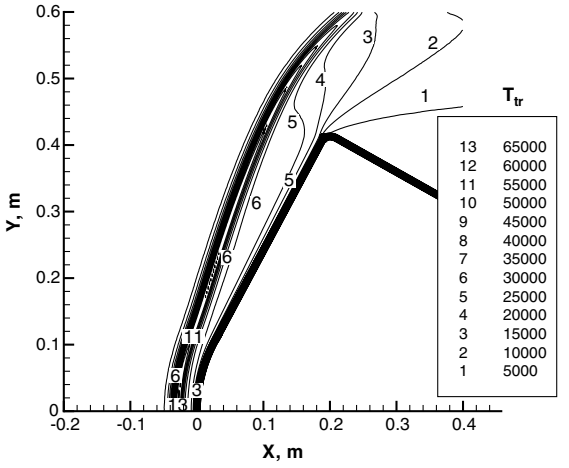

b)

Fig. 10 DSMC contours for the Stardust blunt body at 80 km: a) normalized overall number density, and b) translational temperature.

which is about 21,000 K, is also observed on the shoulder of the Stardust body. Note that, in the modeling of the flow around the blunt body shape of the aeroassist flight experiment [15,45], a similar feature was observed. The reason why a peak in the degree of ionization and thermal excitation occurs off the stagnation point is that the majority of the gas particles pass through a strong shock wave and flow around the body without being cooled by collisions with the surface. Because they travel a greater distance through the shock layer than those particles that flow along the stagnation streamline, they experience a greater number of collisions that result in thermal excitation and chemical reactions. In Fig. 12, the distributions of total, ion, and electron number densities along the stagnation line in DSMC are shown. At 80 km, the DOI is approximately 4% in the stagnation region, with both ions and electrons produced within $x = -0.03$ m of the body. The number density of electrons and ions are nearly the same in the shock region, that is, the charge-neutrality implementation scheme is validated in the shock region.

First, DSMC and CFD with an assumption of $T_e = T_{\text{tr}}$ are compared. Figure 13 presents a comparison of distributions of the translational, rotational, vibrational, and electron temperature along the stagnation line between DSMC and CFD for the case of $T_e = T_{\text{tr}}$. In DSMC, the maximum translational temperature is about 65,000 K along the stagnation line, a value high enough to produce electrons in the shock. It is interesting to note that the electron concentration and translational temperature peaks do not coincide, with the former being closer to the body (see Fig. 12). The delay in electron formation is due to the need for the dissociation and initiation processes (1–3) to occur. This behavior was noted previously by Olynick et al. [4] and others [46,47]. In DSMC, the electron temperature is the same order as the vibrational temperature. However, in the CFD model, due to the assumption of $T_e = T_{\text{tr}}$, CFD predicts much higher electron temperatures than DSMC. As shown in Fig. 14, this resulted in higher electron impact ionization rates. The dominant ionization process is $N + N \rightarrow N_2^+ + e^-$ (2), but further downstream of the shock, process (4) $e^- + N \rightarrow e^- + N^+ + e^-$ dominates. Further downstream of the shock, because of the electron impact ionization processes, N^+ and O^+ concentrations significantly increase in CFD. Compared to 4% in DSMC, CFD predicted as high as 25% DOI along the stagnation line. Furthermore, the higher energy exchange between the translational and internal modes and the dissociation and ionization rates resulted in the lower translational temperature in CFD.

Second, DSMC and CFD with an assumption of $T_e = T_{\text{vib}}$ are compared. Figure 15 presents a comparison of distributions of the translational, rotational, vibrational, and electron temperatures along the stagnation line between DSMC and CFD for the case of $T_e = T_{\text{vib}}$. Compared to Fig. 13 ($T_e = T_{\text{tr}}$ case), the discrepancy between DSMC and CFD is significantly decreased. The maximum

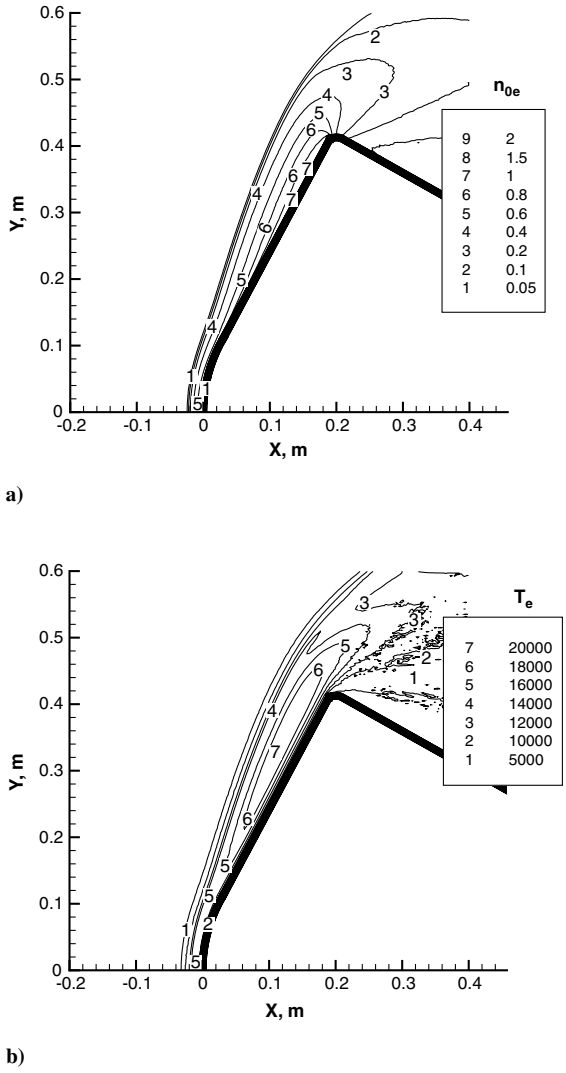

Fig. 11 DSMC contours for the Stardust blunt body at 80 km: a) normalized electron number density, and b) electron temperature.

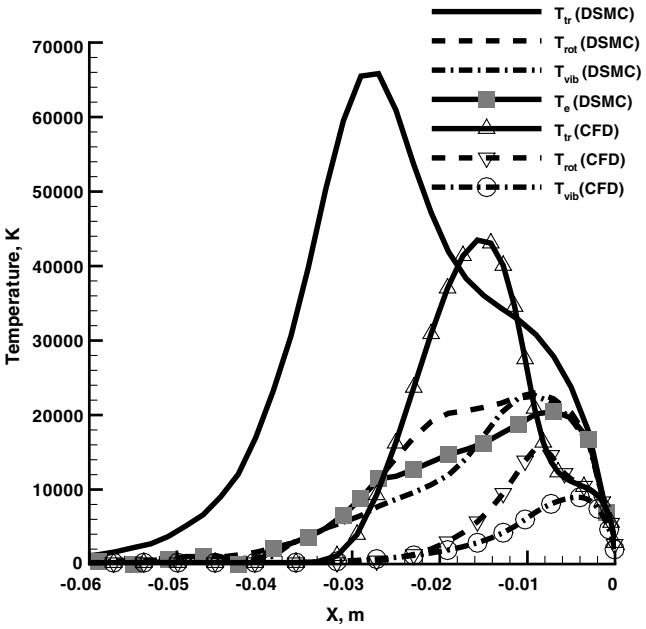

Fig. 13 Comparison of distributions of the translational, rotational, vibrational, and electron temperatures between DSMC and CFD($T_e = T_{tr}$) along the stagnation line at an altitude of 80 km.

translational temperature in CFD is approximately 60,000 K for this case. As shown in Fig. 16, with the assumption of $T_e = T_{vib}$ the rates for the electron impact ionization processes (4) $e^- + N \rightarrow e^- + N^+ + e^-$ and (5) $e^- + O \rightarrow e^- + O^+ + e^-$ are decreased; thus, the energy consumption due to these reactions is much less than the case of $T_e = T_{tr}$. The maximum number density of N^+ and O^+ is about one order of magnitude lower than the $T_e = T_{tr}$ case. This results in the longer shock standoff distance in CFD than that of the $T_e = T_{tr}$ case. The DOI is predicted to be approximately 9% for this case in CFD. This indicates that CFD results are very sensitive to the electron temperature assumption, and by comparing them with the DSMC result, it would be better to set the CFD electron temperature to the vibrational rather than the translational temperature. Because the DSMC calculated T_e separately from T_{vib}, and the TCE chemistry model in DSMC resulted in the different chemistry from CFD, the internal temperatures are higher in DSMC inside the shock, and the DOI is lower than CFD.

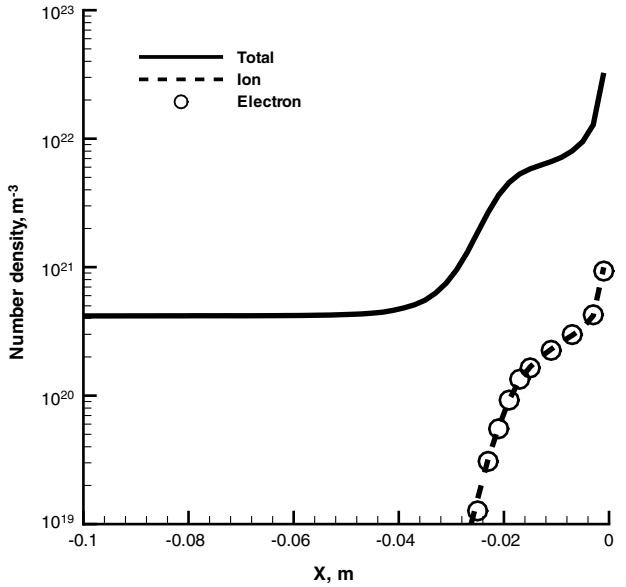

Fig. 12 Distribution of total, ion, and electron number densities in DSMC along the stagnation line for the Stardust-like blunt body at an altitude of 80 km.

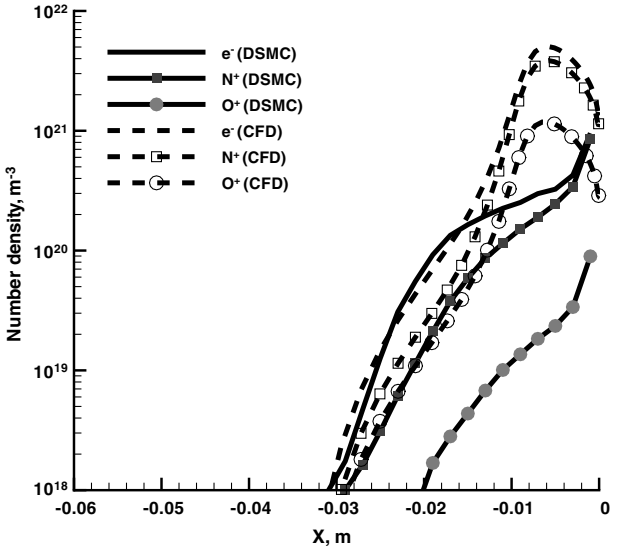

Fig. 14 Comparison of distributions of e^-, N^+, and O^+ number densities between DSMC and CFD($T_e = T_{tr}$) along the stagnation line at an altitude of 80 km.

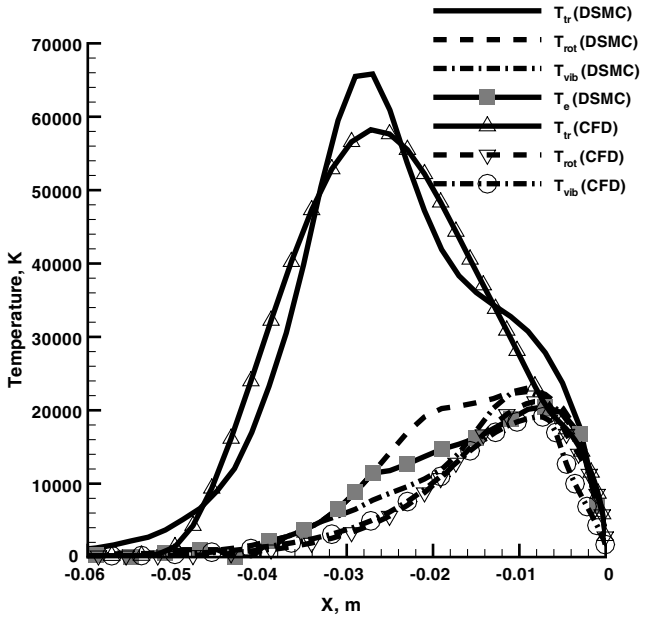

Fig. 15 Comparison of distributions of the translational, rotational, vibrational, and electron temperatures between DSMC and CFD($T_e = T_{\text{vib}}$) along the stagnation line at an altitude of 80 km.

D. Velocity Distribution Function at 80 km

In this subsection, we analyze the DSMC velocity distributions of N_2 and N in the strong shock. Figure 17 shows the velocity distributions of N_2 (left-hand column) and N (right-hand column) at three locations along the stagnation line for the five ionization reaction cases: $(x[\text{m}], y[\text{m}]) = (-0.03, 0.0)$ (top row), $(x, y) = (-0.02, 0.0)$ (middle row), and $(x, y) = (-0.01, 0.0)$ (bottom row). The top figure shows velocity distributions of N_2 and N at $(x[\text{m}], y[\text{m}]) = (-0.03, 0.0)$. The N_2 velocity distributions are representative of the freestream condition, but the N distributions are broader because the source of atomic nitrogen is from the products of dissociation reactions in the shock region. In the freestream, little N exists; thus, the statistical noise is not small. For N_2, in the x direction, the average velocity u_x is 12.8 km/s, and in the y and z directions, the distributions agreed well and $u_y = u_z = 0$. The middle figure shows the distributions in the high gradient region, and the distributions of N_2 can be seen to deviate from a Boltzmann distribution. Because the distribution looks like a two-peak distribution, it can be expressed as a bimodal distribution function [48]. Also, the distribution is so different (i.e., temperature) between the parallel and perpendicular directions to the freestream. Because the effect of deviation from the Boltzmann distribution is so significant in this region, we will discuss a bimodal distribution model in the next subsection. However, the distributions of N have a Boltzmann-like distribution, and there is little directional nonequilibrium because N is a reaction product. Using the BL model, the distribution of the product species is similar to the Boltzmann distribution. The N distributions correspond to temperatures of approximately 80,000 (top), 42,000 (middle), and 29,000 K (bottom). In the bottom row, distributions of N_2 and N are shown inside the shock. Inside the shock, the deviation of N_2 from a Boltzmann distribution and directional nonequilibrium are decreased. For N, the distributions are Boltzmann-like, and the directional nonequilibrium is very small.

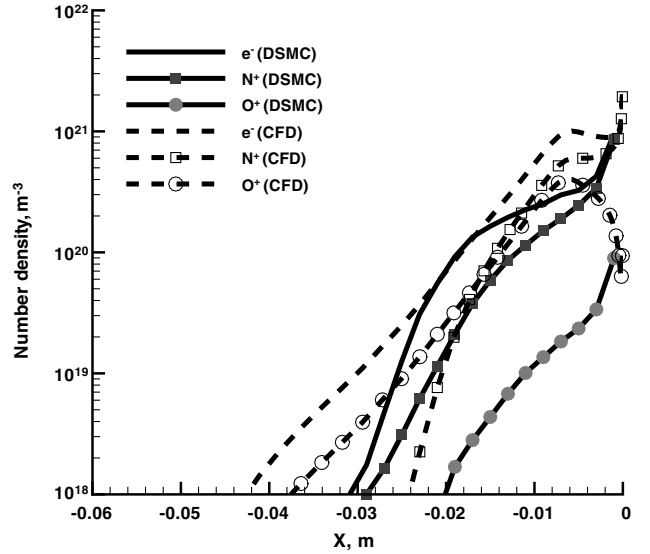

Fig. 16 Comparison of distributions of e^-, N^+, and O^+ number densities between DSMC and CFD($T_e = T_{\text{vib}}$) along the stagnation line at 80 km altitude.

E. Bimodal Distribution Function Model

In a strong shock, the velocity distribution can be characterized by the existence of two maxima of comparable magnitudes. In this subsection, we discuss a bimodal distribution model [48] and compare it with the N_2 distributions obtained from the DSMC calculations. Note that, in the DSMC results, the full charge recombination at the wall was used. The bimodal distribution function g is defined as a weighted sum of the upstream (freestream) f_a and downstream (thermal) f_b distribution functions and can be expressed as [48]

$$g_i = \text{Fr}_{i,a} f_{i,a}(u_{i,a}, T_{i,a}) + \text{Fr}_{i,b} f_{i,b}(u_{i,b}, T_{i,b}) \tag{6}$$

where

$$f_i(u_i, T_i) = \left(\frac{m}{2\pi k_B T_i}\right)^{1/2} \exp\left[-\frac{m(v_i - u_i)^2}{2k_B T_i}\right] \tag{7}$$

The subscript i denotes the x, y, and z directions, and $\text{Fr}_{i,a}$ and $\text{Fr}_{i,b}$ are the fractions of the upstream and downstream contributions, respectively. Because

$$\int_{-\infty}^{\infty} f_i \, \mathrm{d}v_i = 1$$

and

$$\int_{-\infty}^{\infty} g_i \, \mathrm{d}v_i = 1$$

we also must have

$$\text{Fr}_{i,a} + \text{Fr}_{i,b} = 1 \tag{8}$$

Using a curve obtained by a least-squares approximation, eight variables ($\text{Fr}_{i,a}$ in the x and y directions for a, and $\text{Fr}_{i,b}$ u_i, and T_i in the x and y directions for b) at each location were calculated. Note that $u_{i,a}$ and $T_{i,a}$ are already known from the freestream conditions. The calculated bimodal distribution functions for N_2 are compared with the DSMC distributions along the stagnation line in Figs. 18 and 19. The left-hand-side figures show $g(x)$ and the right-hand-side figures show $g(y)$ at $(x[m], y[m]) = (-0.06, 0.0)$, $(-0.03, 0.0)$, $(-0.028, 0.0)$, $(-0.026, 0.0)$, $(-0.024, 0.0)$, $(-0.022, 0.0)$, $(-0.020, 0.0)$, and $(-0.018, 0.0)$. It is shown that the bimodal distribution functions agree very well with the DSMC distributions at each location. In the shock, there are two kinds of particles, one that holds the freestream properties (subscript a), and the other that has experienced collisions (subscript b). The collided particles have a thermal temperature that is much higher than the freestream temperature and have a much lower velocity in the x direction than 12.8 km/s. The ratio of thermally hot particles to freestream particles starts to increase near $x = -0.04$ m, as shown in Fig. 20.

Figure 20 presents the distribution of $\text{Fr}_{x,b}$ and $\text{Fr}_{y,b}$ along the stagnation line. It is found that the change in $\text{Fr}_{x,b}$ and $\text{Fr}_{y,b}$ is very similar between the x and y directions; thus, the fraction of the downstream contribution can be represented by one function. The fraction of the downstream contribution starts to increase near

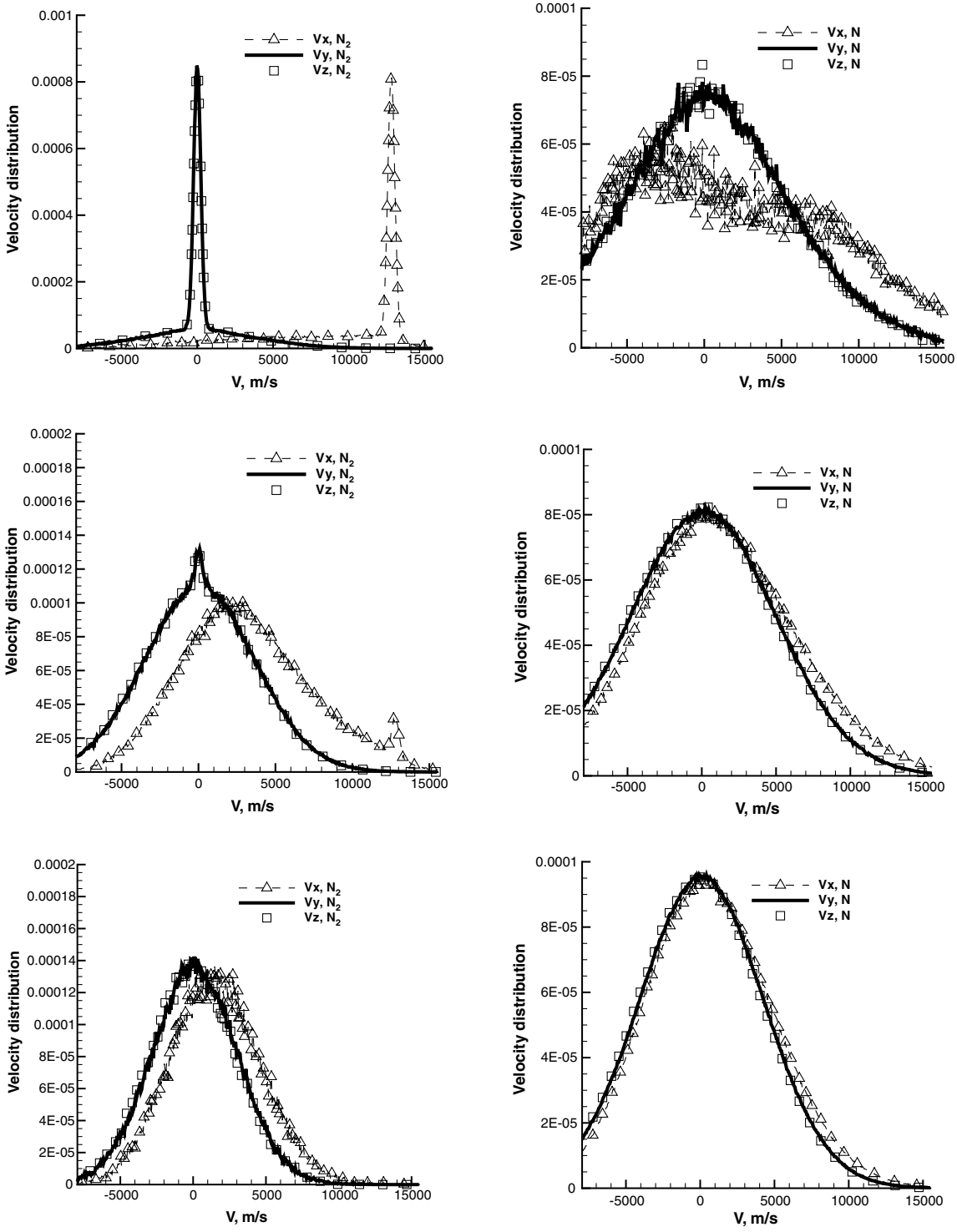

Fig. 17 Velocity distribution function of N_2 (left column) and N (right column) at $(x, y) = (-0.03, 0.0)$ (top row), $(x, y) = (-0.02, 0.0)$ (middle row), and $(x, y) = (-0.01, 0.0)$ (bottom row) for the five ionization reaction cases.

$x = -0.04$ m and becomes unity around $x = -0.02$ m. In addition, the location of the fraction change corresponds to the N_2 number density change in the shock between -0.04 and -0.02 m.

Using these fractions, the average temperature in each direction is obtained as

$$T_{i,\mathrm{av}} = \mathrm{Fr}_{i,a} T_{i,a} + \mathrm{Fr}_{i,b} T_{i,b} \tag{9}$$

and the temperature is averaged over three directions as

$$T_{\mathrm{tr,av}} = (T_{x,\mathrm{av}} + T_{y,\mathrm{av}} + T_{z,\mathrm{av}})/3 \tag{10}$$

In Fig. 21, N_2 translational temperatures in the x and y directions along the stagnation line are shown. The dashed lines denote the downstream temperatures, $T_{i,b}$; the dashed line with the circles denote the averaged temperatures, $T_{i,\mathrm{av}}$; the solid line with the circles denotes $T_{\mathrm{tr,av}}$; and the dashed line with the squares denote the N_2 translational temperature in DSMC. $T_{x,b}$ is as high as 140,000 K in the shock and much higher than $T_{x,a}$. Using the $\mathrm{Fr}_{i,b}$, the maxima of the averaged temperatures become approximately 100,000 in the x direction and 40,000 in the y direction. The overall averaged temperature $T_{\mathrm{tr,av}}$ obtained from the bimodal distribution function model is nearly the same as the DSMC result, and the difference is

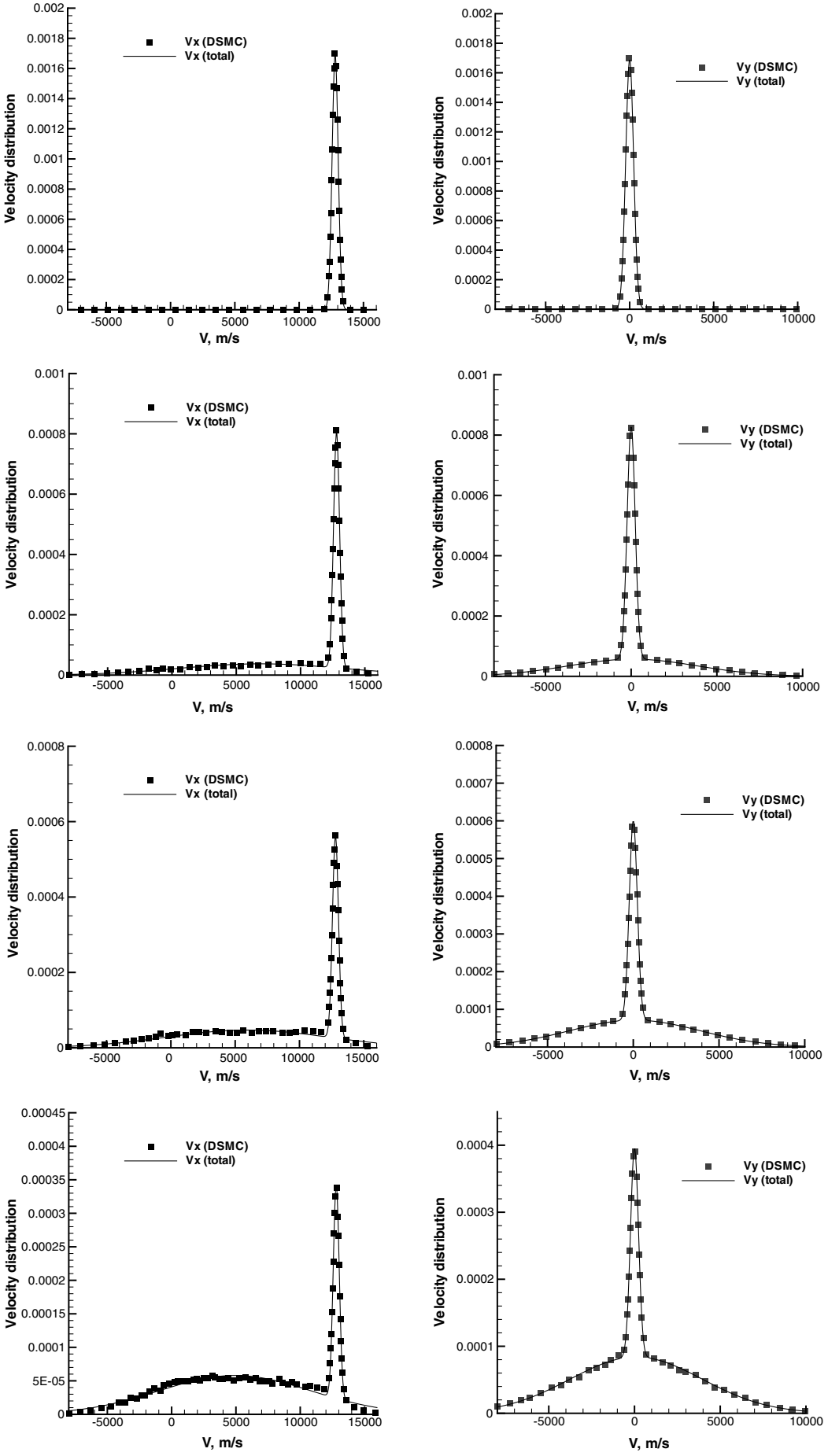

Fig. 18 Velocity distribution function of N_2 in x (left column) and y (right column) at $(x[\mathrm{m}], y[\,]) = (-0.06, 0.0)$ (top row), $(x, y) = (-0.03, 0.0)$ (second row), $(x, y) = (-0.028, 0.0)$ (third row), and $(x, y) = (-0.026, 0.0)$ (bottom row) for the five ionization reaction cases.

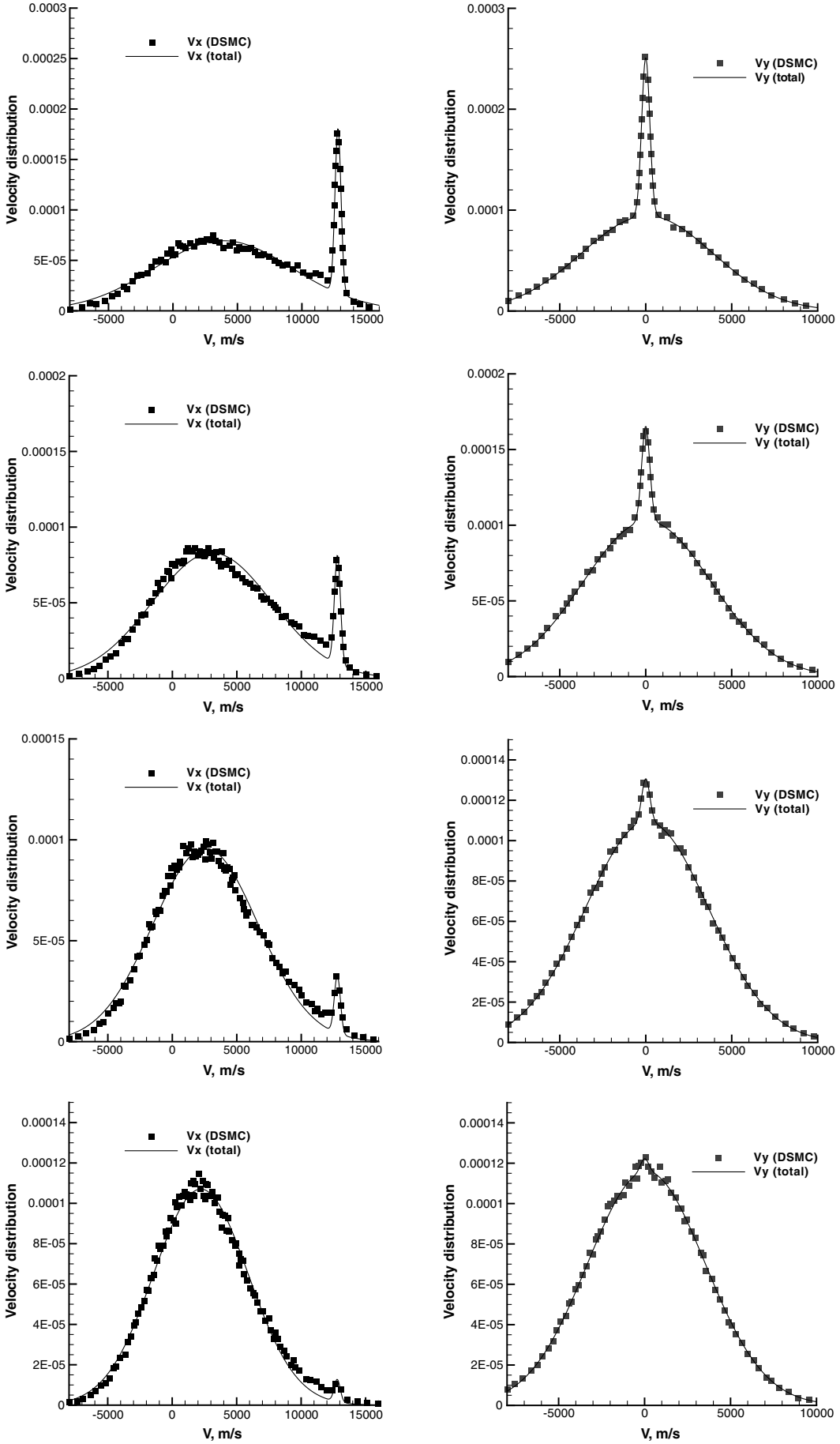

Fig. 19 Velocity distribution function of N_2 in x (left column) and y (right column) at $(x[\mathrm{m}], y[\mathrm{m}]) = (-0.024, 0.0)$ (top row), $(x, y) = (-0.022, 0.0)$ (second row), $(x, y) = (-0.020, 0.0)$ (third row), and $(x, y) = (-0.018, 0.0)$ (bottom row) for the five ionization reaction cases.

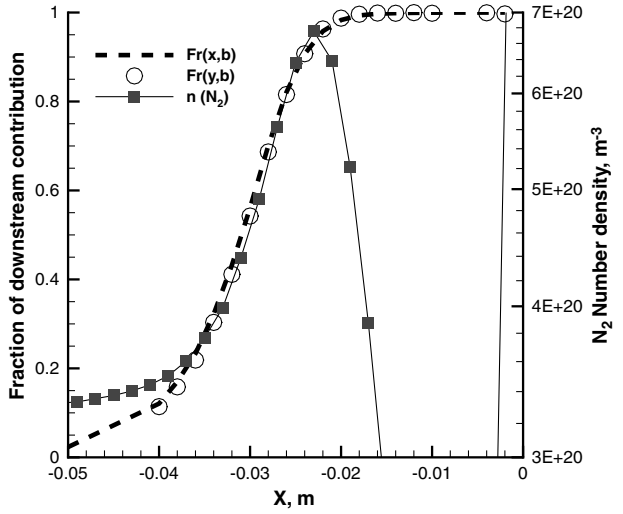

Fig. 20 Distributions of $Fr_{x,b}$ and $Fr_{y,b}$ and number density of N_2 along the stagnation line.

less than 20%. Hence, the bimodal distribution function model is representative of the DSMC calculations.

From the solution of the conservation equations [49], the two fractions $Fr_{i,a}$ and $Fr_{i,b}$ can be obtained in terms of the average local velocity u_i:

$$\mathrm{Fr}_{i,a} = \frac{u_i - u_{i,b}}{u_{i,a} - u_{i,b}}, \qquad \mathrm{Fr}_{i,b} = \frac{u_{i,a} - u_i}{u_{i,a} - u_{i,b}} \tag{11}$$

Solving the equation of transfer and assuming Maxwellian molecules, the average local velocity was obtained by Mott-Smith (M-S) [48] as

$$u_i = u_{i,b} + (u_{i,a} - u_{i,b}) \Big/ \left\{ 1 + \exp\left[\left(1 - \frac{u_{i,b}}{u_{i,a}} \right) \frac{x - x_{\mathrm{center}}}{A_i \lambda_a} \right] \right\} \tag{12}$$

where

$$A_i = \sqrt{\frac{2}{\pi}} \frac{u_{i,b}}{u_{i,a}} \left[\left(1 - 2\frac{u_{i,b}}{u_{i,a}} \right) \frac{u_{i,a}}{\sqrt{k_B T_{i,a}/m}} + 3\frac{\sqrt{k_B T_{i,a}/m}}{u_{i,a}} \right] \tag{13}$$

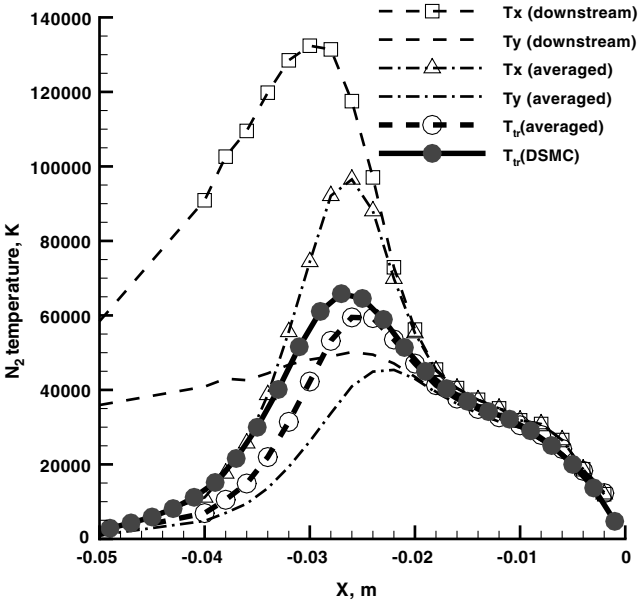

Fig. 21 N_2 translational temperatures in the x and y directions along the stagnation line.

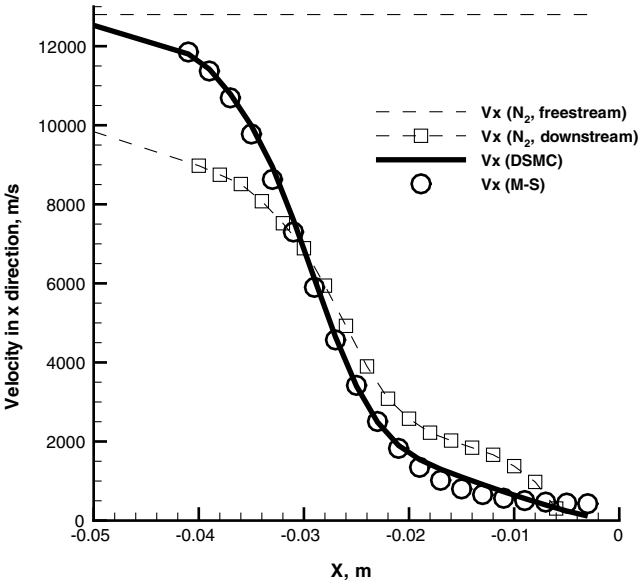

Fig. 22 Comparison of the average local velocity between DSMC and the M-S model along the stagnation line.

In the x direction, the M-S model is used to calculate the fraction of downstream contribution and compared with the fraction obtained earlier directly from the DSMC results. In the freestream, $u_{x,a} = 12.4$ km/s, $T_{x,a} = 185$ K, and $\lambda_a = 3.34 \times 10^{-3}$ m. The value of x_{center} is set equal to -0.03, the location at which the density gradient is the maximum along the stagnation line, and a value of $u_{x,b} = 400$ m/s is used in the equations. Figure 22 shows a comparison of the average local velocity between DSMC and the M-S model along the stagnation line. It is shown that the u_x is gradually decreased from $x = -0.05$ to -0.01 m, and using these values, the velocities obtained by the M-S model, u_i, agree very well with those of DSMC.

Figure 23 shows that the ratio of thermally hot to freestream particles, $Fr_{i,b}$, starts to increase near $x = -0.04$ m. The terms labeled $\mathrm{Fr}(x,b)$ and $\mathrm{Fr}(y,b)$ are computed directly from local distribution functions shown in Figs. 18 and 19. Two other calculations of the fraction of downstream contribution for bimodal distribution functions obtained using Eqs. (11–13) are also shown in the figure. The DSMC velocity is used in Eq. (11) for the third case

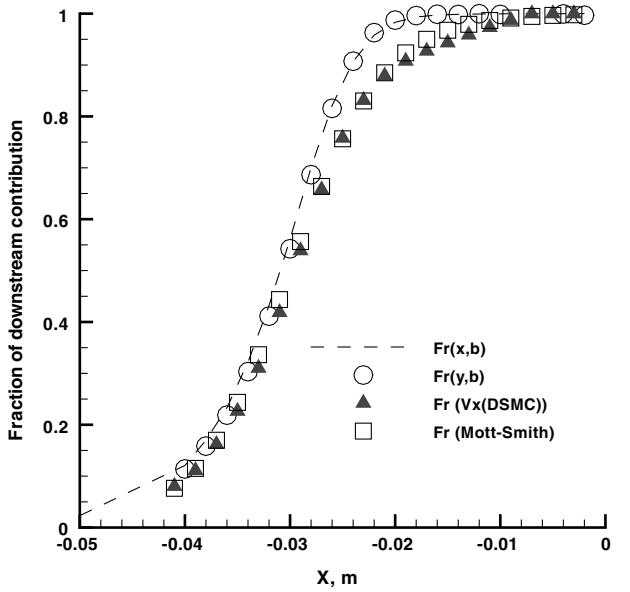

Fig. 23 Fraction of the downstream distribution function contribution for bimodal distribution functions in the M-S model along the stagnation line. The DSMC velocity is used for the third case, labeled $\mathrm{Fr}(V_x(\mathrm{DSMC}))$.

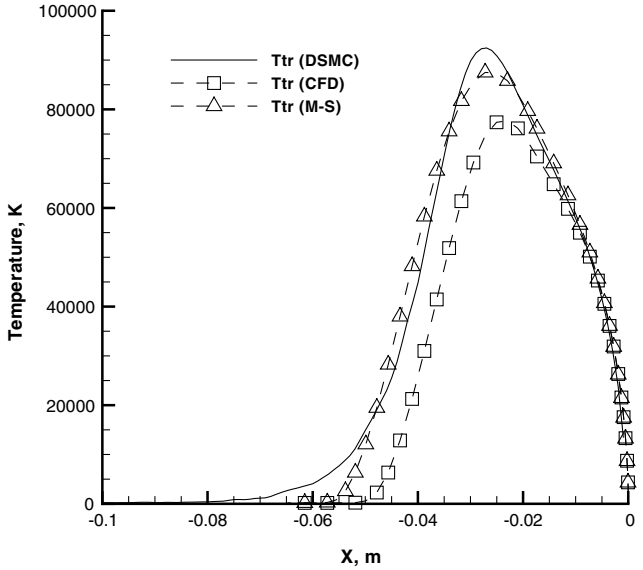

Fig. 24 Comparison of distributions of the translational temperature between CFD results with and without the M-S model for the chemically frozen case along the stagnation line.

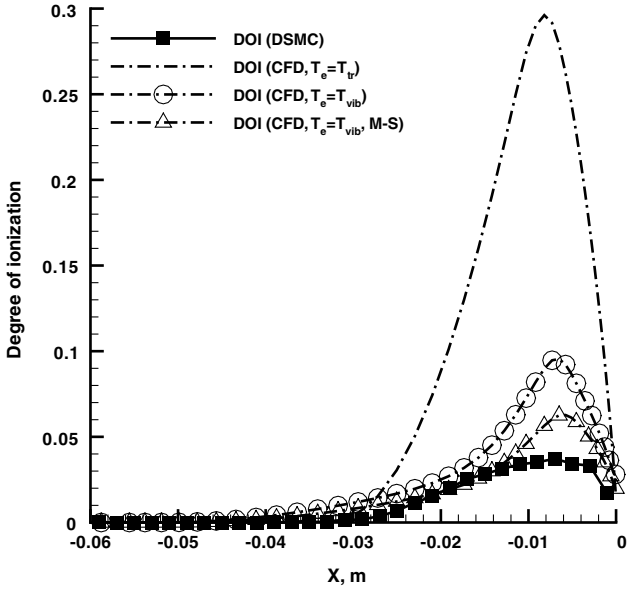

Fig. 26 Comparison of the DOI among DSMC and three CFD results ($T_e = T_{\rm tr}$ and $T_e = T_{\rm vib}$ with and without the M-S model) along the stagnation line.

(labeled Fr(V_x(DSMC))), and u_x is calculated by the M-S model for the fourth case. Using the DSMC velocity, the fraction shows a similar trend to and good agreement with the bimodal distribution functions obtained directly from DSMC. In addition, using the velocity obtained from Eq. (12), the fraction of downstream contribution predicted by the M-S model agrees well with DSMC. Therefore, the M-S model is applicable to this hypersonic flow with Mach numbers greater than 35.

Demonstrations were carried out to show the effect of the M-S model coupling in CFD. To apply the M-S model to the CFD solution, we need to specify $x_{\rm center}$ and $u_{x,b}$. We set $x_{\rm center}$ to the location at which the density gradient is the highest and $u_{x,b}$ to 400 m/s as was shown to give good agreement with the DSMC results. A simple function was obtained to fit with the $x_{\rm center}(y)$ in DSMC and the function is used in CFD. Using the fractions, the average temperature is obtained as $T_{\rm tr,av} = {\rm Fr}_{i,a}T_{{\rm tr},a} + {\rm Fr}_{i,b}T_{{\rm tr},b}$.

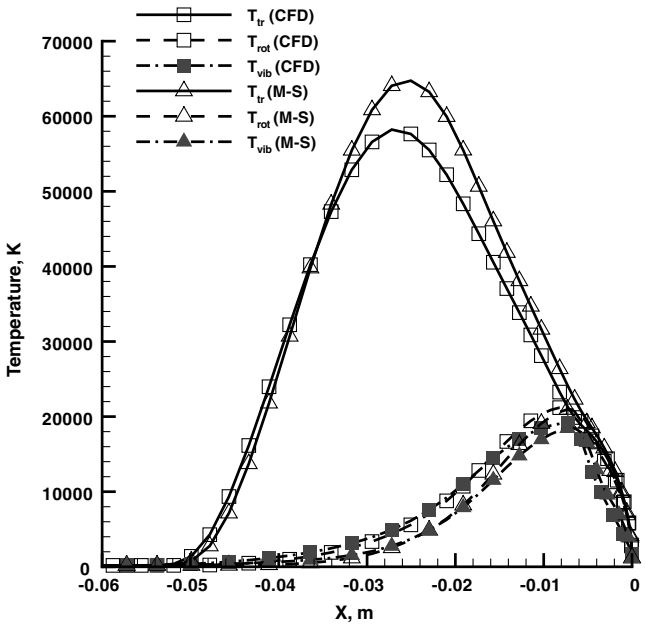

Fig. 25 Comparison of distributions of the translational, rotational, vibrational, and electron temperatures between the CFD results ($T_e = T_{\rm vib}$) with and without the M-S model along the stagnation line.

The averaged temperature, $T_{\rm tr,av}$, obtained from the M-S model was used as an effective temperature, or a replacement for the CFD translational temperature when collisional relaxation or chemical reaction rates were calculated.

First, the M-S model was applied to the chemically frozen case. As you can see in Fig. 9, the discrepancy in the translational temperature distribution between the DSMC and CFD was large for this case. However, it is shown in Fig. 24 that the discrepancy between DSMC and CFD is reduced with the M-S model and the shock standoff distance for the CFD with the M-S model agreed well with DSMC. Because of the freestream contribution to the overall velocity distribution inside the shock, the relaxation was slowed down and the translational temperature was increased.

Second, the M-S model was applied to the full chemical reactions and charged species case. Figure 25 shows a comparison of the distributions of the translational, rotational, and vibrational temperatures along the stagnation line between the cases with and without the M-S model in CFD ($T_e = T_{\rm vib}$). It is seen that for the region far from the body the relaxation was slowed down and the translational temperature was increased. The maximum temperature is the same order as DSMC, and both the rotational and vibrational temperatures in CFD are decreased due to the lower effective temperature in the relaxation model. Thus, the degree of thermal nonequilibrium predicted by the CFD ($T_e = T_{\rm vib}$) case using the M-S model has improved. Note that there still remain differences in the temperature assumption and chemistry models between the CFD and DSMC calculations. Finally, a comparison of the DOI among the four cases, DSMC and three CFD results ($T_e = T_{\rm tr}$ and $T_e = T_{\rm vib}$ with and without the M-S model), is presented in Fig. 26. With the M-S model, the DOI for the case of $T_e = T_{\rm vib}$ in CFD becomes approximately 6% and is decreased by approximately 3%. The M-S model also influences the chemistry inside the shock as well as the relaxation rates and results in lower ionization rates. However, the assumption of $T_e = T_{\rm vib}$ was found to be more crucial in CFD compared with the case of $T_e = T_{\rm tr}$.

IV. Conclusions

Hypersonic flows were simulated for the Stardust blunt body at an altitude of 80 km using the DSMC and CFD methods, and the two methods were discussed for a high nonequilibrium case. Five ions and electrons were considered in the flowfield, and ionization processes were modeled in DSMC. Electrons were moved in the flowfield using the charge-neutrality assumption and the IAV method

was validated to maintain charge neutrality. Collision and energy-exchange models for DSMC were reviewed to ensure adequacy for the high-energy flow regime. The VHS model parameters were revisited to use high-temperature viscosity data because it was found that the shock thickness for an artificial gas consisting only of atomic N is sensitive to the degree of viscosity in the total collision cross section. Because electron-heavy particle collisions occur approximately a hundred times more frequently than collisions between heavy particles, the adequacy of the VHS model in representing the total collision cross section for electron-heavy particle collisions was also examined. Accurate electron-heavy particle collision cross sections based on atomic and molecular collision data were implemented. Moreover, the e-V energy-exchange model using Lee's relaxation time is included in DSMC.

With 12.8 km/s, DSMC results agreed well with CFD for the collision-only case. However, with the relaxation model activated, the discrepancy between DSMC and CFD was found in the shock, and relaxation was found to be sensitive to the breakdown effect.

Furthermore, with full chemical reactions and ionization processes, DSMC results were compared with CFD results. At 80 km, whereas the DOI in DSMC was predicted to be approximately 4% along the stagnation line, the DOI is greater than 25% for the case of $T_e = T_{\text{tr}}$ and 9% for the case of $T_e = T_{\text{vib}}$ in CFD. Although the $\text{N} + \text{O} \rightarrow \text{NO}^+ + \text{e}^-$ reaction is the most important initiation process for electron formation, electron impact ionization reactions become dominant further downstream of the shock and N^+ is the dominant ion inside the shock. At this altitude, the flow is highly nonequilibrium; thus, the electron temperature assumption is crucial to predicting electron impact ionization rates and DOI. In DSMC, the e-V relaxation model was found to be important to predict electron and vibrational temperatures at this altitude, and the electron temperature is the same order as the vibrational temperature. Therefore, compared to the DSMC solution, the assumption of $T_e = T_{\text{vib}}$ is preferable in CFD.

In addition, DSMC velocity distributions were investigated in the shock. It was found that the DSMC distributions in the shock could be represented by the bimodal distribution functions. Also, using the M-S model, good agreement was obtained between the analytical bimodal distribution functions and DSMC results for the Stardust reentry flows.

Finally, a correction of effective temperature in the relaxation and chemical reaction models in CFD was proposed using the M-S model, and demonstrations were implemented. Considering the freestream contribution in the velocity distribution, the CFD solution was improved. With the M-S model, the CFD translational temperature was increased and the maximum became the same order as DSMC. The DOI also decreased by approximately 3% for the Stardust reentry case at 80 km, and the discrepancy between DSMC and CFD was reduced, slowing down the relaxation and chemical relaxation rates inside the shock. Although CFD still predicts two times higher DOI than DSMC near the body, it was found that the assumption of $T_e = T_{\text{vib}}$ was the most crucial in CFD and the M-S model usage has improved the CFD solution.

Acknowledgments

The research performed at Pennsylvania State University was supported by the NASA Ames Research Center through the Eloret agreement no. 85224 entitled "Stardust Post-Flight Data Analysis." Special thanks are to M. Ivanov of the Institute of Theoretical and Applied Mechanics, Russia, for the use of the original SMILE code. We also would like to acknowledge H. Deng for computational help.

References

[1] Ozawa, T., Zhong, J., and Levin, D. A., "Development of Kinetic-Based Energy Exchange Models For Non-Continuum, Ionized Hypersonic Flows," *Physics of Fluids*, Vol. 20, No. 4, 2008, p. 046102. doi:10.1063/1.2907198

[2] Ayasoufi, A., Rahmani, R. K., Cheng, G., Koomullil, R., and Neroorkar, K., "Numerical Simulation of Ablation for Reentry Vehicles," AIAA Paper 2006-2908, June 2006.

[3] Zhong, J., Ozawa, T., and Levin, D. A., "Modeling of Stardust Reentry Ablation Flows in the Near-Continuum Flight Regime," *AIAA Journal*, Vol. 46, No. 10, Oct. 2008, pp. 2568–2581. doi:10.2514/1.36196

[4] Olynick, D., Chen, Y.-K., and Tauber, M. E., "Aerothermodynamics of the Stardust Sample Return Capsule," *Journal of Spacecraft and Rockets*, Vol. 36, No. 3, 1999, pp. 442–462. doi:10.2514/2.3466

[5] Ozawa, T., Zhong, J., Levin, D. A., Boger, D. A., and Wright, M., "Modeling of the Stardust Reentry Flows with Ionization in DSMC," AIAA Paper 2007-0611, Jan. 2007.

[6] Ozawa, T., Nompelis, I., Levin, D. A., Barnhardt, M., and Candler, G. V., "DSMC-CFD Comparison of a High Altitude, Extreme-Mach Number Reentry Flow," AIAA Paper 2008-1216, Jan. 2008.

[7] Boyd, I. D., "Monte Carlo Simulation of Nonequilibrium Flow in a Low-Power Hydrogen Arcjet," *Physics of Fluids*, Vol. 9, No. 10, 1997, pp. 3086–3095. doi:10.1063/1.869474

[8] Bird, G. A., *Molecular Gas Dynamics and the Direct Simulation of Gas Flows*, Clarendon, Oxford, England, U.K., 1994.

[9] Park, C., "Problems of Rate Chemistry in the Flight Regimes of Aeroassisted Orbital Transfer Vehicles," *Thermal Design of Aeroassisted Orbital Transfer Vehicles*, edited by H. F. Nelson, Vol. 96, AIAA, New York, 1985, pp. 511–537.

[10] Park, C., "Assessment of Two-Temperature Kinetic Model for Ionizing Air," *Journal of Thermophysics and Heat Transfer*, Vol. 3, No. 3, 1989, pp. 233–244. doi:10.2514/3.28771

[11] Boyd, I. D., and Chen, G., "Prediction Failure of the Continuum Fluid Equations in Transitional Hypersonic Flows," *Physics of Fluids*, Vol. 7, No. 1, 1995, pp. 210–219. doi:10.1063/1.868720

[12] Schwartzentruber, T. E., Scalabrin, L. C., and Boyd, I. D., "Modular Implementation of a Hybrid DSMC-NS Algorithm for Hypersonic Non-Equilibrium Flows," AIAA Paper 2007-613, Jan. 2007.

[13] Candler, G. V., Nijhawan, S., and Bose, D., "A Multiple Translational Temperature Gas Dynamics Model," *Physics of Fluids*, Vol. 6, No. 11, 1994, pp. 3776–3786. doi:10.1063/1.868367

[14] Wang, W.-L., and Boyd, I. D., "Predicting Continuum Breakdown in Hypersonic Viscous Flows," *Physics of Fluids*, Vol. 15, No. 1, 2003, pp. 91–100. doi:10.1063/1.1524183

[15] Candler, G. V., "The Computation of Weakly Ionized Hypersonic Flows in Thermo-Chemical Nonequilibrium," Ph.D. Thesis, Stanford Univ., Palo Alto, CA, 1988.

[16] Nompelis, I., Drayna, T. W., and Candler, G. V., "A Parallel Unstructured Implicit Solver for Hypersonic Reacting Flow Simulation," AIAA Paper 2005-4867, June 2005.

[17] Bird, G. A., "Monte-Carlo Simulation in an Engineering Context," *Rarefied Gas Dynamics*, edited by S. Fisher, Vol. 74, AIAA, New York, 1981, pp. 239–255.

[18] Park, C., *Nonequilibrium Hypersonic Aerothermodynamics*, Wiley, New York, 1990.

[19] Bird, G. A., "Nonequilibrium Radiation During Re-Entry at 10 km/s," AIAA Paper 87-1543, June 1987.

[20] Ivanov, M. S., Markelov, G. N., and Gimelshein, S. F., "Statistical Simulation of Reactive Rarefied Flows: Numerical Approach and Applications," AIAA Paper 1998-2669, June 1998.

[21] Ivanov, M. S., and Rogasinsky, S. V., "Analysis of the Numerical Techniques of the Direct Simulation Monte Carlo Method in the Rarefied Gas Dynamics," *Soviet Journal of Numerical Analysis and Mathematical Modelling*, Vol. 3, No. 6, 1988, pp. 453–465. doi:10.1515/rnam.1988.3.6.453

[22] Bird, G. A., "Direct Simulation of Typical AOTV Entry Flows," AIAA Paper 86-1310, June 1986.

[23] Millikan, R. C., and White, D. R., "Systematics of Vibrational Relaxation," *Journal of Chemical Physics*, Vol. 39, No. 12, 1963, pp. 3209–3213. doi:10.1063/1.1734182

[24] Parker, J. G., "Rotational and Vibrational Relaxation in Diatomic Gases," *Physics of Fluids*, Vol. 2, No. 4, 1959, pp. 449–462. doi:10.1063/1.1724417

[25] Lee, J. H., "Electron-Impact Vibrational Excitation Rates in the Flowfield of Aeroassisted Orbital Transfer Vehicles," *Thermophysical Aspects of Reentry Flows*, edited by J. N. Moss and C. D. Scott, Vol. 103, AIAA, New York, 1986, pp. 197–224.

[26] Lee, J. H., "Electron-Impact Vibrational Relaxation in High-Temperature Nitrogen," *Journal of Thermophysics and Heat Transfer*,

Vol. 7, No. 3, Sept. 1993, pp. 399–405.
doi:10.2514/3.432

[27] Lumpkin, F. E., Haas, B. L., and Boyd, I. D., "Resolution of Differences Between Collision Number Definition in Particle and Continuum Simulations," *Physics of Fluids. A, Fluid Dynamics*, Vol. 3, No. 9, 1991, pp. 2282–2284.
doi:10.1063/1.857964

[28] Haas, B. L., Hash, D. B., Bird, G. A., Lumpkin, F. E., and Hassan, H. A., "Rates of Thermal Relaxation in Direct Simulation Monte Carlo Methods," *Physics of Fluids*, Vol. 6, No. 6, 1994, pp. 2191–2201.
doi:10.1063/1.868221

[29] Blaha, M., and Davis, J., "Elastic Scattering of Electrons by Oxygen and Nitrogen at Intermediate Energies," *Physical Review A*, Vol. 12, No. 6, 1975, pp. 2319–2324.
doi:10.1103/PhysRevA.12.2319

[30] Thomas, L. D., and Nesbet, R. K., "Low Energy Electron Scattering by Atomic Nitrogen," *Physical Review A*, Vol. 12, No. 6, 1975, pp. 2369–2377.
doi:10.1103/PhysRevA.12.2369

[31] Kennerly, R. E., "Absolute Total Electron Scattering Cross Sections for N_2 Between 0.5 and 50 eV," *Physical Review A*, Vol. 21, No. 6, 1980, pp. 1876–1883.
doi:10.1103/PhysRevA.21.1876

[32] Morrison, M. A., Saha, B. C., and Gibson, T. L., "Electron-N_2 Scattering Calculations with a Parameter-Free Model Polarization Potential," *Physical Review A*, Vol. 36, No. 8, 1987, pp. 3682–3698.
doi:10.1103/PhysRevA.36.3682

[33] Morrison, M. A., Saha, B. C., and Gibson, T. L., "Ultrasimple Calculation of Very-Low-Energy Momentum-Transfer and Rotational-Excitation Cross Sections: e-N_2 Scattering," *Physical Review A*, Vol. 55, No. 4, 1997, pp. 2786–2798.
doi:10.1103/PhysRevA.55.2786

[34] Itikawa, Y., and Ichimura, A., "Cross Sections for Collisions of Electrons and Photons with Atomic Oxygen," *Journal of Physical and Chemical Reference Data*, Vol. 19, No. 3, 1990, pp. 637–651.
doi:10.1063/1.555857

[35] Kanik, I., Nickel, J. C., and Trajmar, S., "Total Electron Scattering Cross Section Measurements for Kr, O_2 and CO," *Journal of Physics. B, Atomic, Molecular and Optical Physics*, Vol. 25, No. 9, May 1992, pp. 2189–2196.
doi:10.1088/0953-4075/25/9/022

[36] Alle, D. T., Brennan, M. J., and Buckman, S. J., "Low-Energy Total Electron Scattering Cross Section and Electron Affinity for NO," *Journal of Physics. B, Atomic, Molecular and Optical Physics*, Vol. 29, No. 7, 1996, pp. L277–L282.
doi:10.1088/0953-4075/29/7/006

[37] Szmytkowski, C., and Maciag, K., "Total Cross Section for Electron Impact on Nitrogen Monoxide," *Journal of Physics. B, Atomic, Molecular and Optical Physics*, Vol. 24, No. 19, 1991, pp. 4273–4279.
doi:10.1088/0953-4075/24/19/021

[38] Bird, G. A., "Simulation of Multi-Dimensional and Chemically Reacting Flows," *Rarefied Gas Dynamics*, edited by R. Campargue, AIAA, New York, 1979, pp. 365–388.

[39] Wright, M., Candler, G. V., and Bose, D., "Data-Parallel Line Relaxation Method for the Navier–Stokes Equations," *AIAA Journal*, Vol. 36, No. 9, 1998, pp. 1603–1609.
doi:10.2514/2.586

[40] Candler, G. V., and MacCormack, R. W., "Computation of Weakly Ionized Hypersonic Flows in Thermochemical Nonequilibrium," *Journal of Thermophysics and Heat Transfer*, Vol. 5, No. 3, 1991, pp. 266–273.
doi:10.2514/3.260

[41] Palmer, G. E., and Wright, M. J., "Comparison of Methods to Compute High-Temperature Gas Viscosity," *Journal of Thermophysics and Heat Transfer*, Vol. 17, No. 2, 2003, pp. 232–239.
doi:10.2514/2.6756

[42] Svehla, R. A., "Estimated Viscosities and Thermal Conductivities of Gases at High Temperatures," NASA TR R-132, 1962.

[43] Stallcop, J. R., Partridge, H., and Levin, E., "Effective Potential Energies and Transport Cross Sections for Interactions of Hydrogen and Nitrogen," *Physical Review A*, Vol. 62, No. 6, Nov. 2000, p. 062709.
doi:10.1103/PhysRevA.62.062709

[44] Wright, M., Bose, D., Palmer, G. E., and Levin, E., "Recommended Collision Integrals for Transport Property Computations, Part 1: Air Species," *AIAA Journal*, Vol. 43, No. 12, 2005, pp. 2558–2564.
doi:10.2514/1.16713

[45] Candler, G., and Park, C., "The Computation of Radiation from Nonequilibrium Hypersonic Flows," AIAA Paper 1988-2678, June 1988.

[46] Greendyke, R. B., Gnoffo, P. A., and Lawrence, R. W., "Calculated Electron Number Density Profiles for the Aeroassist Flight Experiment," *Journal of Spacecraft and Rockets*, Vol. 29, No. 5, 1992, pp. 621–626.
doi:10.2514/3.11501

[47] Taylor, J. C., Carlson, A. B., and Hassan, H. A., "Monte Carlo Simulation of Radiating Re-Entry Flows," *Journal of Thermophysics and Heat Transfer*, Vol. 8, No. 3, 1994, pp. 478–485.
doi:10.2514/3.568

[48] Mott-Smith, H. M., "The Solution of the Boltzmann Equation for a Shock Wave," *Physical Review*, Vol. 82, No. 6, 1951, pp. 885–892.
doi:10.1103/PhysRev.82.885

[49] Vincenti, W. G., and Kruger, C. H. J., *Introduction to Physical Gas Dynamics*, Wiley, New York, 1965.